

Scheduled to appear in AJ, December, 2003

The Recent Evolution of the Dwarf Starburst Galaxy NGC 625 from Hubble Space Telescope Imaging¹

John M. Cannon, Robbie C. Dohm-Palmer and Evan D. Skillman

*Department of Astronomy, University of Minnesota,
116 Church St. S.E., Minneapolis, MN 55455*

cannon@astro.umn.edu, rdpalmer@astro.umn.edu, skillman@astro.umn.edu

Dominik J. Bomans

*Astronomisches Institut, Ruhr-Universität Bochum,
Universitätsstr. 150, 44780 Bochum, Germany*

bomans@astro.ruhr-uni-bochum.de

Stéphanie Côté

*Canadian Gemini Office, Herzberg Institute of Astrophysics,
National Research Council of Canada,
5071 West Saanich Road, Victoria, BC, Canada, V9E 2E7*

stephanie.cote@nrc.ca

Bryan W. Miller

Gemini Observatory, Casilla 603, La Serena, Chile

bmilller@gemini.edu

ABSTRACT

New HST/WFPC2 imaging of the dwarf starburst galaxy NGC 625 is presented. These data, which are 80% complete to V and I magnitudes of 26.0 and 25.3 respectively, allow us to study the recent star formation history of NGC 625. Using outlying red giant stars, we derive a tip of the red giant branch (TRGB) distance modulus of 27.95 ± 0.07 . This corresponds to a distance of 3.89 ± 0.22 Mpc, placing this system on the far side of the Sculptor Group. NGC 625 has a well-defined radial stellar population gradient, evidenced by a central concentration of young main sequence stars and an RGB/AGB ratio that increases with galactocentric distance. The prominent AGB is very red, similar to the population found in the Local Group dIrr NGC 6822. The RGB stars

can be detected out far from the central star forming activity and show an elliptical distribution in agreement with the galaxy’s outer H I distribution.

Using H α and H β narrow band imaging and previous optical spectroscopy we identify substantial and varying internal extinction associated with the central active star formation regions. This extinction, which varies from $A_V = 0.0$ to 0.6 magnitudes, hampers efforts to derive a detailed recent star formation history. To better understand the effects of internal extinction on the analysis of young stellar populations, synthetic models are presented which, for the first time, examine and account for this effect. Using the luminous blue helium burning stars, we construct a simple model of the recent (< 100 Myr) star formation in which an elevated but declining star formation rate has been present over this entire period. This is at odds with the presence of spectroscopic W–R features in the major star formation region which imply a short duration (≤ 5 Myr) for the recent starburst. This suggests that starbursts displaying W–R features are not necessarily all of a short duration. Finally, we speculate on the possible causes of the present burst of star formation in this apparently isolated galaxy, and compare it to other nearby, well-studied dwarf starburst systems.

Subject headings: galaxies: evolution — galaxies: irregular — galaxies: starburst — galaxies: dwarf — galaxies: individual (NGC 625)

1. Introduction

Nearby dwarf star-forming galaxies serve as important benchmarks in theories of the formation of galaxies at high redshifts, and therefore are vital laboratories in which the process of star formation can be studied at high spatial resolution (Hodge 1989, Mateo 1998, and references therein). Detailed studies of these galaxies can help to answer many questions not only about the process of star formation itself, but also about the process of structure formation. By observing signatures of the star formation process in such galaxies, where large-scale galactic dynamics are absent or less important than in spiral galaxies, we can attempt to gauge the importance of stochastic processes in the evolution of low-mass star-forming galaxies.

In particular, by observing the resolved stellar populations of such objects, we can directly derive their recent star formation histories. This information allows us to constrain the nature of the star formation processes that have been dominant recently, including duration and strength of bursts, fiducial sizes and masses of star formation regions, and the temporal and spatial behavior of star formation throughout the galaxy. We can then place the galaxies into context amongst

¹Based on observations with the NASA/ESA Hubble Space Telescope, obtained at the Space Telescope Science Institute, which is operated by the Association of Universities for Research in Astronomy, Inc. under NASA contract No. NAS5-26555.

different classes of star-forming galaxies. For example, very active starburst episodes might place star-forming galaxies in the class of blue compact dwarfs (BCD’s - Searle & Sargent 1972; Searle, Sargent, & Bagnuolo 1973). A star formation history that is less bursty in nature might be more representative of the class of dIrr galaxies. Environmental factors likely also play an important role in the evolution of dwarf galaxies (see, e.g., Skillman, Côté, & Miller 2003a (hereafter SCM03a), and references therein), but these effects are not yet fully understood. For example, location in a dense environment might result in a heightened present or recent star formation rate, or the distinctive signature of ram pressure stripping (e.g., Bureau & Carignan 2002).

NGC 625 is an intriguing nearby dwarf galaxy in the Sculptor Group (or South Polar Group), the nearest group of galaxies outside the Local Group (Karachentsev et al. 2003, and references therein). The spectroscopic studies of Marlowe et al. (1997; hereafter MMHS) and Marlowe, Meurer, & Heckman (1999) revealed strong starburst activity, with values of star formation rate and $H\alpha$ equivalent width comparable to (but less than) those found in the prototypical local dwarf starbursts NGC 1705 and NGC 5253. The ROSAT discovery of faint x-ray emission (Bomans & Grant 1998) implied a large content of hot ($T \sim 10^6$ K) gas in the halo. Coupled with the ground-based $H\alpha$ imaging of SCM03a and new XMM-NEWTON imaging of the galaxy (Bomans, Cannon, & Skillman 2003), diffuse $H\alpha$ emission is detected away from the disk and coincident with the soft x-ray emission. This leads to the interesting conclusion that this nearby galaxy is likely driving an outflow of hot gas from the major star formation region. In Table 1, we summarize salient properties of the galaxy, as drawn from the literature.

As this low-mass galaxy presents a low-foreground reddening sightline to a nearby major star formation region, it serves as an ideal galaxy in which to study the starburst phenomenon in its own right. We adopt the definition of Heckman (1998), where a starburst galaxy is any system that contains a spatially concentrated star formation region that dominates the overall luminosity of the galaxy, and that implies a gas depletion timescale much shorter than the age of the universe. Starbursts are thus a brief but important site for massive star formation locally ($\gtrsim 25\%$ of massive star formation occurring therein; Heckman 1998), and may have been even more important in previous epochs. They play an integral role in the evolution of galaxies through their interaction with the ISM. Furthermore, these galaxies represent a link between star formation and environment, as many are triggered by interactions, and some appear to vent metals into the IGM (e.g., NGC 1569; Martin, Kobulnicky, & Heckman 2002). Thus, NGC 625 is a representative laboratory for the investigation of the details of an important mode of the star formation process. In § 9 we draw further comparisons between NGC 625 and nearby starbursts.

This paper is organized as follows. In § 2 we describe the observations and data reduction procedures, and in § 3 the analysis is presented. The distance of the galaxy is derived from the tip of the red giant branch in § 4. In § 5 we discuss the models used to analyze the recovered photometry, the methods used to isolate the various stellar populations within NGC 625, and our new method of simulating the effects of differential extinction in stellar populations. We address the young and old stellar populations, respectively, in §§ 6 & 7, with particular attention paid to

the rigorous burst of star formation which this relatively isolated galaxy is undergoing, and the simulations used to interpret this young stellar population. In § 8 we speculate on the triggering mechanism of the current starburst episode, in § 9 we compare NGC 625 with other dwarf starburst systems, and finally in § 10 we draw conclusions about starburst galaxies in general and NGC 625 in particular.

2. Observations and Data Reduction

NGC 625 was observed with the Wide Field/Planetary Camera 2 (WFPC2) aboard the Hubble Space Telescope (HST) on 2000, September 23 & 24. Images were obtained in four different passbands: V (F555W filter, 5200 sec), I (F814W filter, 10400 sec), $H\alpha$ (F656N filter, 800 sec) and $H\beta$ (F487N filter, 1200 sec). Table 2 summarizes the data obtained. Figure 1 shows the HST/WFPC2 field of view superposed on a ground-based R-band image. The brightest central clusters were centered on the PC chip to minimize stellar crowding. The field of view encompasses most of the central disk and much of the eastern halo of the galaxy, allowing the study of stellar populations in both field and star-forming regions. No dithering strategy was applied during the data acquisition. The images were processed through the standard pipeline reductions at STScI.

2.1. Broad Band Images

The images were combined into single exposures for each passband by applying the anti-coincidence routine of Saha et al. (1996) to remove cosmic ray detections between pairs of images. The success of this method, which uses a moderate rejection threshold (4σ), requires multiple pairs of images in each filter. All images were obtained at the same pointing, mitigating the need for aligning successive images. Further reductions were not applied to the broad band images before their analysis (e.g., removal of background levels); rather, the automated photometry routines applied (see § 3) account for such effects. A four-color composite image is presented in Figure 2. Note the high stellar density in the disk, and the major starburst region which is displaced toward the eastern end of the disk. Note also the clear presence of nebular emission and dust obscuration.

2.2. Narrow Band Images

The reduction and calibration of the narrow band images followed the methodology outlined in Cannon et al. (2002). We need to quantify potentially subtle features (e.g., variations in the $H\alpha/H\beta$ flux ratio), thus requiring great care that the calibration be as precise as possible. For consistency, the broad band images used for the continuum subtraction (see below) were re-reduced via the same prescription applied to the narrow band images.

The images were first corrected for warm pixel effects and geometric distortion. Cosmic rays were removed via the IRAF² task CRREJ, which is reasonably effective with only two images, as for the F656N (H α) and F487N (H β) images. However, some cosmic rays were not filtered out and these were removed manually. An average background level was determined for each chip and then subtracted. Due to the large extent of the galaxy, estimating the background is difficult for the broad band images (particularly for the PC1 and WF2). Fortunately, due to the small contribution of the underlying stellar continuum (see below), this error term will be of second order. We discuss below the overall accuracy of our narrow band calibration, and its total error budget.

The broad band images were flux calibrated using standard methods. For the narrow band images, the system responses of the filters at the redshifted wavelengths of the emission lines were modeled with the SYNPHOT package. We adopt a heliocentric radial velocity of 405 km sec⁻¹ for NGC 625, derived from the H I synthesis imaging of Côté, Carignan, & Freeman (2000; hereafter CCF00). The narrow band images were then corrected for differences in throughput at these wavelengths compared to the nominal values at the band centers.

In narrow band analysis, removing the underlying stellar continuum is often the most difficult step of the analysis. Dutil & Roy (2001) suggest that, regardless of quality and signal-to-noise ratio of the data, the precision of continuum subtraction cannot be better than 2% in H α and 4% in H β . The most effective method is suggested to be the simple “manual method”, and should be preferred to more sophisticated techniques, such as χ^2 minimization. In the present analysis we apply a variant of this technique, which is described as follows.

The F555W image is contaminated by both H α and H β emission, while the F814W bandpass is not sensitive to either line. Following Cannon et al. (2002) and Dutil & Roy (2001), the continuum subtraction was thus achieved recursively by scaling and subtracting the images (i.e, manually). When the scaled narrow band images were subtracted from the wide band images, we considered the continuum optimally removed when there no longer remained significant regions of nebular contamination in the wide band filter. We attach the aforementioned 4% uncertainty to this value (see § 3 for a description of the errors that affect the narrow band images).

The continuum-subtracted narrow band images were then multiplied by the effective filter widths as calculated by SYNPHOT. The final, continuum-subtracted emission line images are presented in Figures 3(a) and 3(b). Note that the H β image, while a longer integration, presents the lowest signal-to-noise ratio (and statistically dominant error term, see § 3). Comparison to ground-based H α studies lends confidence to our calibration. Our derived total H α flux of $(3.49 \pm 0.18) \times 10^{-12}$ erg sec⁻¹ cm⁻² agrees well with that found by SCM03a $((3.3 \pm 0.2) \times 10^{-12}$ erg sec⁻¹ cm⁻²) and by MMHS $(3.3 \times 10^{-12}$ erg sec⁻¹ cm⁻²).

²IRAF is distributed by the National Optical Astronomy Observatories, which are operated by AURA, Inc., under cooperative agreement with the National Science Foundation.

3. Analysis

3.1. Stellar Photometry

The DoPHOT program (Schechter, Mateo, & Saha 1993), with modifications for the under-sampled WFPC2 pixels (Saha et al. 1996), was used to derive the photometry of the individual stars in the V and I images. The subtleties involved in applying DoPHOT to crowded WFPC2 images have been discussed at length in Dohm-Palmer et al. (1997a) and Dohm-Palmer et al. (2002), to which we refer the interested reader for specific details.

As an inspection of Figure 2 will reveal, the stellar crowding is high in the center of the galaxy, most noticeably in the PC and WF2 chips. In an effort to curtail the detrimental effects of crowding, DoPHOT subtracts an analytically defined, scaled point spread function (PSF) from the image at each star’s location. Highly crowded areas will be susceptible to errors in this process, as subtraction residuals can be mistaken for stars.

DoPHOT’s analytic PSF fitting function is controlled by four parameters: β_4 , β_6 , β_8 , and the FWHM. Following Dohm-Palmer et al. (1997a), these parameters are fitted to the brightest, most isolated stars in each chip. The PSF is determined by minimizing the residuals of subtractions of isolated stars from the images. The best results were found by allowing small variations in FWHM from chip to chip, but using the same values for β_4 , β_6 and β_8 as derived in Dohm-Palmer et al. (2002). These shape parameters are given explicitly in Table 3.

Aperture corrections were next performed on the DoPHOT outputs. Corrections were measured in an aperture of $0.5''$ for stars with small internal DoPHOT errors (≤ 0.04 mag in I, ≤ 0.08 mag in V). The high crowding levels in some chips made it difficult to isolate numerous stars of such quality, and in some cases, the aperture correction for a chip had to be based on a relatively small number of stars. A polynomial function (quadratic in position) was then fit to these derived values. Table 3 lists the number of stars used to calculate the aperture correction per chip, and the rms residual of the fit. As expected, the PC chips have the highest rms value, due to the highest levels of crowding found there.

Charge transfer efficiency (CTE) corrections were applied according to the prescription of Whitmore, Heyer, & Casertano (1999) (which is in general agreement with the more recent calibration by Dolphin (2000)). Photometry lists in V and I were next matched to a radius of 0.5 pixels. In total, 52,188 stars were matched between the two filters. More stringent cuts in these data (based on total errors in V and I magnitude) will be used in the analysis that follows, reducing the number of stars used to derive the star formation history. Finally, the transformation to the V and I magnitude system was found via the equations given in Holtzman et al. (1995, which is in good agreement with Dolphin 2000). The complete I vs. (V–I) and V vs. (V–I) color magnitude diagrams for all detected stars are shown in Figure 4.

At the high galactic latitude of -73° , the foreground reddening toward NGC 625 is expected

to be low. The maps of Schlegel, Finkbeiner, & Davis (1998; hereafter SFD98) find a value of $E(B-V) = 0.016$, which we adopt in the following analysis (see also § 3.3). Applying the extinction coefficients from the same work yields $A_V = 3.25 \cdot E(B-V) = 0.05$ mag, and $A_I = 1.95 \cdot E(B-V) = 0.03$ mag. These corrections have been applied to the calibrated photometry presented here, and a 10% error on the A_λ values propagated (although this error is usually negligible compared to the internal DoPHOT photometric errors).

Foreground stellar contamination is also expected to be minimal; the models of Ratnatunga & Bahcall (1985) predict a contamination of 2.3 stars arcmin⁻² (brighter than 27th magnitude in V) for the nearest appropriate globular cluster (NGC 4147; 21° offset). For the usable field of view of the WFPC2 camera, we then expect ~ 12 stars to contaminate the CMD of NGC 625. Thus, we conclude that such contamination is negligible for the analysis at hand.

In Figure 5, we present the total photometric errors for all matched stars between I and V (including errors from the foreground reddening correction). The V data are roughly one magnitude deeper than the I data. The larger errors and greater spread of this distribution toward faint magnitudes is expected. The large number of stars which scatter above this trend is due to the high stellar density and crowding throughout some regions of the images.

To test the completeness of our photometry, artificial star tests were performed. The V-band luminosity function was found to fit a power law with exponent 0.44. Artificial stars were created according to the analytic function which was used to fit the bright, isolated stars in each image. Stars randomly distributed with this power-law distribution in V magnitude were then added at the 2% level to 100 copies of each image. These stars were randomly distributed in position. Each random distribution was applied to both the V and I images, with (V-I) colors randomly assigned between -1 and 2 . Poisson noise was then added to each artificial star.

DoPHOT was applied to each of the artificial images using identical parameters to those used in the science frames. The input star lists and the artificial frame photometry were then matched, and the fraction of recovered stars was measured as a function of magnitude. Due to the steep stellar density gradient present in some sections of the galaxy, the resulting completeness estimates are calculated as a function of stellar density. These calculations are discussed in the next section.

3.2. Isolating Crowding Effects

Some sections of the the V and I images suffer from severe stellar crowding, which will have detrimental effects on the recovered photometry. Furthermore, the steep stellar gradient between the disk and the halo results in deeper photometry in the outer parts of the galaxy. In order to isolate and minimize these effects, we break up the photometry into annular regions which will have relatively equal amounts of stellar crowding and background variation. This analysis allows us to isolate crowding effects with a fair degree of accuracy.

In analyzing the stellar photometry, we follow the general method adopted by Tosi et al. (2001) in their study of the starburst galaxy NGC 1705. Here we separate the CMD into sections using elliptical contours of a fixed axial ratio (2.8:1) guided by isophotal fits to the images. This elliptical contour analysis allows us to study the distribution of stars with respect to the main disk of the galaxy. This will be very important, for example, in the determination of the distance from the TRGB (see § 4) and in the study of the spatial distribution of the various stellar populations found throughout the galaxy (see §§ 6 & 7).

The contours used to divide the photometry are displayed in Figure 6. The galaxy is divided into six regions. The outer stars in the periphery of the galaxy are included in Region 1. Crowding levels increase as one approaches the main disk of the galaxy. Region 6 contains the highest stellar densities, as well as the large H II regions listed in Table 4 and the dust concentrations discussed in § 3.3 and listed in Table 5. The individual color magnitude diagrams for each section of the galaxy are shown in Figure 7.

From an inspection of Figure 7, it is clear that these areas not only isolate similar crowding levels, but also similar age progressions of the stellar populations contained within. The blue plume, which consists of main sequence (MS) and blue helium burning stars (BHeB), is prominent in Regions 5 and 6, and decreases in strength as one moves away from the main disk (toward Regions 2 and 1). The very red asymptotic giant branch (AGB) is evident in all regions, but most easily identifiable in the regions further from the disk (Regions 1 and 2, for example). The implications of such a spatial distribution are discussed in more detail in §§ 6 & 7. The red giant branch (RGB) is most easily isolated in the outer regions (see § 4), and becomes confused with the faint end of the red supergiant population in regions closer to the main disk of the galaxy.

In order to compare the stellar distributions in each of the annuli, we must consider the relative completeness of the photometry in each region. Figure 7 shows that the inner regions, where stellar crowding is most severe, suffer from relatively high incompleteness. By separating our artificial star simulations into the same regions used to analyze the photometry, we determine that Region 6 becomes incomplete at 0.5 (V) and 1.2 (I) magnitudes shallower than Region 1. In Figure 7 we include the results of the completeness tests for each of the six regions (also discussed further in §§ 6 & 7).

Aparicio et al. (1996) emphasize that detailed crowding effects must be included in the distribution of artificial stars which is input into the images. By separating the analysis of our observations into annuli of similar stellar densities (i.e., separate photometric errors and completeness measurements) we can accomplish the same goal. Since our analysis will concentrate on stars that are primarily above the completeness limits of the photometry (e.g., red giants, and younger stars in the blue plume) completeness estimates are not critical to most of our interpretation.

3.3. Narrow Band Photometry

The narrow band images were analyzed with two goals in mind. First, we can study the distribution of $H\alpha$ emission in comparison with the distribution of young stars. Second, in tandem with the $H\beta$ image, we can map the large-scale effects of reddening throughout the disk. This will help us to correct the CMD analysis of the affected populations.

Due to the intrinsically lower background levels, the effects of charge transfer efficiency must be carefully considered in the analysis of HST narrow band imaging. However, because of the small area of the CCD covered by the nebular emission, the prescriptions of Whitmore et al. (1999) and Dolphin (2000) both give correction terms of order 1% over the extent of the features in both $H\alpha$ and $H\beta$, as seen in Figure 3. The effects of these corrections are negligible compared to the errors inherent in the subtraction of the continuum (see below), so pixel-by-pixel CTE corrections were not applied to the narrow band images considered here. As previously mentioned, the foreground reddening toward NGC 625 is low, $E(B-V) = 0.016$ mag. This foreground correction has been applied to the narrow band images.

SCM03a, using ground-based images, catalog 23 H II regions in NGC 625. Because of the higher spatial resolution (and hence lower surface brightness sensitivity) of the WFPC2 camera, only the four brightest H II regions are detected (our regions A, B, C, D correspond (roughly) to their H II regions 5, 9, 18, 4, respectively). The properties of these four H II regions are listed in Table 4. The four H II regions account for roughly 95% of the total $H\alpha$ flux recovered from the entire galaxy. We note that these four H II regions also account for over 90% of the total $H\alpha$ flux found in the ground based study. This agreement suggests that the lower surface brightness H II regions found in ground-based images have not been recovered here, and that the nature of the unrecovered $H\alpha$ is mostly discrete, low surface brightness H II regions, rather than a diffuse background. While we cannot completely rule out a diffuse component (perhaps as large as 5 - 10% within our errors), this fraction is small in comparison with the larger diffuse component (10 - 30%) inferred for some gas rich dwarf irregulars (e.g., van Zee 2000; Kennicutt & Skillman 2001).

We then analyze the continuum-subtracted $H\alpha$ and $H\beta$ images via aperture photometry to address the potential contribution from internal (and possibly highly variant) extinction. Apertures are used to attain emission line fluxes in areas of high equivalent width in both the $H\alpha$ and $H\beta$ images. From inspection of Figure 3(b), it is clear that the low signal to noise ratio of the $H\beta$ image will limit our ability to use this technique on a widespread basis throughout the galaxy. We list in Table 5 the recovered photometry for the H II regions delineated in Figure 3(b). Each H II region shows roughly 0.5 magnitudes of extinction at V. These values are consistent with the higher values found in the spectroscopic observations of Skillman, Côté, & Miller (2003b; hereafter SCM03b), where $H\alpha/H\beta$ ratios are elevated above the theoretical value of 2.85 (Hummer & Storey 1987) to as high as 3.6. However, the spectra of SCM03b indicate that one of the H II regions is consistent with no reddening at all. This suggests the presence of variable extinction within the star formation regions. To test for this effect, we separated the areas of high $H\beta$ equivalent width

into sections, and performed aperture photometry on each smaller area individually. We find that extinction levels vary by ~ 0.2 magnitudes over regions as small as $1''$ (18.9 pc at the distance derived in § 4) in the central star formation complexes.

The presence of strong underlying stellar absorption can mimic the behavior of dust extinction. The large (aperture-averaged) equivalent widths derived here (see Table 5), however, suggest that underlying stellar absorption plays only a minor role in elevating our observed $H\alpha/H\beta$ ratios from the theoretical value, and that it is a negligible effect. The models of González Delgado, Leitherer, & Heckman (1999) demonstrate that the contribution from underlying absorption rises with age of the ionizing cluster, and may be as large as $\sim 10 \text{ \AA}$ for clusters which are hundreds of millions of years old. However, the luminosity and equivalent width of the nebular emission argues for a much younger age, with typical contributions from underlying absorption of order 3 \AA , representing less than a 1% effect. Thus, we conclude that the bulk of the elevated $H\alpha/H\beta$ ratio is a consequence of (highly variable) dust extinction along sightlines into the active star formation regions. This varying extinction will cause our stellar photometry to be spread out in color and magnitude; while we may measure a star with small photometric errors in the central regions, this does not necessarily mean that we recover its true absolute magnitude. We argue later (see § 5) that this effect widens our CMD features, rendering our ability to separate different stellar populations less accurate than it would otherwise be in the presence of little (or smoothly varying) extinction.

It has been shown by Zaritsky (1999) and Zaritsky et al. (2002) for the Magellanic Clouds, and by Calzetti (2001) for starburst galaxies, that the contributions to internal extinction are dependent on the population being analyzed. For the Magellanic Clouds, extinctions are of order several tenths of a magnitude larger in the young populations, while variations as large as one magnitude are found in starburst galaxies (e.g., NGC 5253; Calzetti et al. 1997). Since we only have two-color information, we cannot address this issue in detail, but our general results using the $H\alpha/H\beta$ ratio seem to favor such an interpretation. Individual line-of-sight corrections for this effect are not applied; however, we note the potential uncertainty introduced as a result. The effects of differential extinction could be widespread throughout the disk and not necessarily confined to the regions where we have measured them. This is discussed further in § 5. Furthermore, we note that this correction applies in the direction of increasing the luminosities of the individual stars, and therefore, not accounting for this effect will result in older ages and lower star formation rates calculated from MS and BHeB stars.

4. Tip of the Red Giant Branch Distance

The tip of the first ascent red giant branch (TRGB) has been empirically shown to be a useful distance indicator for resolved, metal-poor stellar populations (Lee, Freedman, & Madore 1993; Madore & Freedman 1995; Sakai, Madore, & Freedman 1996; Bellazzini, Ferraro, & Pancino 2001). The relative insensitivity of this CMD feature to metallicity (see below) suggests that TRGB distances are robust and may be reliably applied when other primary indicators are not available.

One assumption in applying the TRGB method is that the red stellar population is old ($\gtrsim 2$ Gyr); however, this assumption is met in every galaxy near enough for its older stellar population to be resolved (see the more detailed discussion in § 7.1).

In nearby galaxies, the agreement between the TRGB distance and the distance derived from variable stars is excellent (Sakai et al. 1996 compare the Cepheid distance with the TRGB distance in Sextans A; Dolphin et al. 2001 compare Cepheid and RR Lyrae distances with the TRGB estimate in IC 1613). In a more extensive comparison of the TRGB with various distance indicators, Ferrarese et al. (2000) find that in all 13 galaxies included in their sample with both TRGB and Cepheid distance estimates, these two distance indicators agree within the total respective errors. These and other results place the TRGB distance indicator on a reliable observational footing as a well-calibrated Population II secondary distance indicator.

We calculate the location of the TRGB using only the stars at large radial distance (Region 1 in Figure 6) from the center of NGC 625. This increases our photometric depth and reduces pollution by crowded faint stars that may blend together to mimic red giants in the central regions of the galaxy. This region is free from recent star star formation and contains essentially only stars in the RGB region of the CMD. Figure 8 shows the resulting I-band luminosity function of the recovered stars in this region, binned in 0.05 magnitude intervals. Note the steep breaks in the I-band luminosity function at $I \approx 23$ and $I \approx 24$ seen in both Figure 8 and the CMD of Region 1 shown in Figure 7. The break at $I \approx 23$ is a textbook quality example of the *false* TRGB due to population I AGB stars (c.f., Saha et al. 1995), and provides a reminder why it is important to observe to more than 1 magnitude below the TRGB for a secure distance determination.

In Figure 8, the I-band luminosity function discontinuity at $I \approx 24$ indicates the TRGB for NGC 625. We adopt the value of $m_{TRGB} = 23.95 \pm 0.07$, and assume zero internal extinction for these stars. Applying the theoretical and empirical calibrations of the TRGB absolute magnitude (Lee et al. 1993; Madore & Freedman 1995; Bellazzini et al. 2001), we use the relation $M_I = -4.0 \pm 0.10$, which should be valid for the metallicity range $-2.8 \leq [\text{Fe}/\text{H}] \leq -0.6$. This will most certainly encompass the metallicity of the old stellar population in NGC 625. From nebular spectroscopy of the major H II regions, SCM03b find a weighted mean metallicity of $12 + \log(\text{O}/\text{H}) = 8.14 \pm 0.02$ ($\sim 28\%$ of Z_\odot , or $Z = 0.006$, adopting the solar oxygen abundance of Allende Prieto, Lambert, & Asplund 2001). This provides an upper limit on the metallicity of the old stellar population, so the above range is well-justified. Applying the metallicity-color relation derived in Da Costa & Armandroff (1990) and also used in Bellazzini et al. (2001), we find that the mean color of the TRGB in NGC 625 is $(V-I)_0 = 1.39$. This then corresponds to a mean $[\text{Fe}/\text{H}]$ at the TRGB of -2.02 , and to an I-band absolute magnitude safely within the above quoted range. Thus, it is not necessary to apply a significant correction to the assumed TRGB value of $M_I = -4.0 \pm 0.10$. The distance of NGC 625 is then found to be 3.89 ± 0.22 Mpc, placing it on the distant side of the three-dimensional structure of the Sculptor Group. This is significantly more distant than the estimate of 2.7 Mpc by Karachentsev et al. (2003) using a Tully-Fisher relation, although they note that this is an uncertain estimate from their expanded radial velocity – distance relation.

5. Stellar Populations, Evolutionary & Synthetic Models

5.1. Identification of Stellar Populations and Comparison to Stellar Evolution Models

The derivation of quantitative star formation histories depends upon comparison of observed data with theoretical isochrones describing the evolution of stars of different masses. Here, we use the stellar evolution models of the Padua group (Bertelli et al. 1994; hereafter B94). In order to conduct a first assessment, a representative value for the stellar metallicity of the dominant stellar population is required. For this, we rely upon two different lines of evidence to estimate the stellar metallicity range in NGC 625. First, as previously mentioned, the mean nebular abundance in NGC 625 is found to be $12+\log(\text{O}/\text{H}) = 8.14\pm 0.02$ (SCM03b). Of course, the older stellar population should have a metallicity lower than the current ISM. Here, we adopt the $Z=0.004$ isochrones of B94. We note that these isochrones fit data on the stellar content of NGC 6822 (which has similar global characteristics and nebular abundance to NGC 625) quite well (see, e.g., Gallart et al. 1994).

This choice of metallicity is supported by the presence of the very red, extended AGB (see § 7.2) which generally only appears in stellar evolution models with $Z \gtrsim 0.001$. Furthermore, the MS and BHeB stars align better with the $Z = 0.004$ models than with the $Z = 0.001$ models. For these reasons, we adopt the $Z = 0.004$ isochrones for the remainder of this work, and use them to determine, quantitatively in the case of the young stars and qualitatively in the case of the older stars, information about the recent star formation history of NGC 625. These isochrones are overlaid on the recovered photometry in Figure 9. Note the good agreement of the 1-6 Gyr isochrones with the red, extended AGB stars detected at $(V-I)$ colors > 1.5 .

The photometry was next separated into four regions (MS, BHeB, RGB, & AGB) by placing selection polygons into the observed CMD. These regions are based on the $Z = 0.004$ theoretical stellar isochrones discussed previously. For the young MS stars, the width of this regions was found by calculating the average error of the color index as a function of magnitude for stars with $(V-I)$ color index < 1.0 . For the BHeB stars, a detailed simulation was performed, including the effects of differential extinction, to determine the locus of points which make up the BHeB sequence. This model is described in detail in § 5.2. Note that the constant-color red edge of the MS selection region is driven by the need to assure exclusive populations between MS and BHeB stars; since the MS stars are not used for quantitative calculations of the star formation history, this will only affect the derived spatial distribution of MS stars. Selection regions for the older stars were created by hand. In an attempt to only retain the RGB stars, our RGB selection region was guided by the photometry for Regions 1 & 2 (see Figure 7), which contain predominantly old stars that are well-separated from the main disk of the galaxy. Finally, the selection region for the AGB stars was guided by noting the position of the AGB in the aforementioned models, and by selecting stars which follow the locus of points for older stars (ages $\sim 1-6$ Gyr) delineated therein. This region then effectively avoids the densely populated red region of the RGB, which, being near the edge of

our photometry, will have relatively high photometric errors.

5.2. Modeling Differential Extinction in Young Stellar Populations

The differential extinction, which blurs the MS and BHeB stars in the CMD, makes our photometric separation of these populations difficult. To better gauge the severity of this effect, in Figure 10 we show a closer view of the Region 6 photometry. Overlaid are the zero-age MS and the sequence showing the blue extent of the core helium burning stars. Note that the wide distribution in color of the young stars argues for pronounced extinction along some (but not necessarily all) sightlines. Coupled with our narrowband imaging, where small-scale variations in the extinction were measured over distances as small as tens of parsecs, we conclude that differential extinction is non-negligible. This effect must be accurately accounted for before a realistic separation of these sequences (which are separated by ~ 0.3 magnitudes in $(V-I)$) can be made.

To explore the effects of differential extinction in detail, we performed simulations of star formation events using the aforementioned stellar evolution models of B94. Here, an initial star formation rate and event duration are specified. Stars are then “created” according to a power-law distribution in mass that is governed by the IMF (here, a Salpeter IMF was applied), and then assigned an age (depending on the length of the star formation event). The temporal resolution is set at 10^5 years, assuring that the short-lived stages of stellar evolution considered here (RGB, red helium burning (RHeB) and BHeB stages) are extractable. Note that MS luminosity evolution is explicitly accounted for.

These stars, now having an age and a mass, are converted into the V vs. $(V-I)$ plane by interpolation over the model grid. Comparing the ages of these stars to model ages of various stellar evolution phases, one can then uniquely determine its position in the CMD. Furthermore, the temporal resolution assures that one can extract synthetic stars in the stages of interest here, namely the MS and BHeB stars. The results of this interpolation produce synthetic photometry representing various stellar populations, including evolving MS stars, red giants, BHeB and RHeB stars.

After this photometry is created, a simple random number generating routine is used to apply first differential extinction and then photometric errors to the synthetic data. Based on our extinction measurements, a flat distribution in differential extinction over the range of $0.0 < A_V < 0.6$ is assumed. Using least-squares fitting to these points in the V vs. $(V-I)$ plane, the location of the BHeB selection region can then be derived. As will be described in § 6.3, these simulations are also used to self-consistently measure the degree of contamination of the BHeB selection regions by reddened MS stars.

The result of this photometric selection process is to produce different visualizations of the distribution of stars of various ages and evolutionary phases throughout the galaxy. In Figure 11 we show the selection regions used to extract the populations (see above for further details). Note

for the BHeB selection region that the diagonal appearance of the region boundaries comes from stars moving down and to the right in the V vs. $(V-I)$ plane as a result of differential extinction (see also § 6.3). Figure 12 presents density plots of the various stellar populations, showing the number of detected stars $\cdot \text{kpc}^{-2}$. We detect a very clear age segregation (i.e., a stellar population gradient) in NGC 625: the young stars (MS, BHeB) are highly concentrated toward the disk, and align well with the locations of star formation (as evidenced by $H\alpha$ emission; see § 6.1) and high-column density H I emission. Note, however, that the largest star formation region (NGC 625 A) does not coincide exactly with the position of the highest column density H I emission (CCF00), but is offset to the east by roughly 300 pc. In contrast to the young stars, as the age of the stellar population increases (AGB stars, RGB stars), the distribution of stars becomes much more diffuse and uniform throughout the galaxy. Each of these facets of the stellar populations of NGC 625 will be discussed in the sections that follow.

6. The Young Stars and Recent Star Formation History

Our WFPC2 data allow us to study both the newly formed stars and the older stellar population of NGC 625. While the orientation of the WFPC2 field of view does not encompass all of the galaxy (see Figures 1 and 2), we do have a representative view of the central and eastern half of the main disk (including all of the major star formation regions), as well as the surrounding halo region. In this section we discuss the recent star formation history of NGC 625 that can be discerned from our data. We discuss both the MS stars and BHeB stars in this context, and use the latter to derive a simple model of the recent star formation history of NGC 625.

6.1. The Main Sequence Stars

Figure 10 demonstrates that MS stars with ages approaching 20 Myr can be identified in our photometry (with the previously noted ambiguity due to differential reddening). The spatial distribution of young (i.e., blue plume) stars is highly concentrated toward the central disk of NGC 625. As Figures 12(a) and 12(b) reveal, the young stars are predominantly located near the large H II complexes, with the bulk of both populations highly concentrated near the largest star formation region (NGC 625 A, see Figure 3). Not all of the MS stars are associated with detected H II regions, however; many are located quite far away from the lowest levels of detected $H\alpha$ emission. To better visualize the spatial coincidence of the detected MS stars and the locations of the major active star formation regions (i.e., those demonstrating $H\alpha$ emission), we plot in Figure 13 the locations of all of the stars identified as young MS stars ($M_V < -2.5$; see Figure 11) which lie in the central region compared with contours of the $H\alpha$ emission. The most luminous regions, NGC 625 A and B, are both associated with many detected MS stars, while NGC 625 C is associated with fewer recovered MS stars, in line with expectations due to its lower $H\alpha$ flux.

The spatial correlation between MS stars and $H\alpha$ emission is biased by the low $H\alpha$ surface brightness sensitivity of the HST (relative to lower angular resolution ground based imaging) resulting in non-detections of known H II regions. While the undetected emission is a small fraction of the total $H\alpha$ emission in NGC 625, it does affect the comparison of MS star locations with $H\alpha$ emission. Figure 1 of SCM03a reveals a large number of smaller H II regions throughout the disk of NGC 625 which we do not detect here, and which most likely are associated with the MS stars which we detect in the present photometric analysis. Low-surface brightness $H\alpha$ emission is present throughout (and slightly beyond) the field of view shown in Figure 13. The fact that some MS stars are associated with lower-surface brightness H II regions (or none at all) suggests that recent star formation has been widespread throughout the central area, and not necessarily confined to the large associations detected here.

6.2. The Blue Helium Burning Stars

Figure 10 demonstrates that BHeB stars with ages approaching 200 Myr can be identified in our photometry (with the previously noted ambiguities due to differential reddening and the confusion with reddened MS stars). Like the MS stars, the distribution of BHeB stars is concentrated toward the disk, although slightly more extended. This could either represent more extended prior star formation or diffusion from natal formation sites, although the former seems more likely, based on typical stellar diffusion velocities. Interestingly, an extension of young stars to the SE is detected prominently in the BHeB stars (see Figure 12b). This region shows that recent star formation was not confined to just the central, high-H I column density regions of NGC 625. The recent enhanced star formation appears to have been more of a distributed as opposed to concentrated phenomenon.

6.3. A Preliminary Model for the Recent Star Formation History of NGC 625

As discussed in § 5, the effects of differential extinction are larger than the theoretical separation of the MS and BHeB stars in the blue plume. Thus, a detailed recent star formation history derived directly from the BHeB luminosity function (e.g., Dohm-Palmer et al. 1997b, 2002) is not straightforward. On the other hand, given the uncertainties introduced by the differential reddening and the increased photometric depth that would be required to reach even moderate ages (at least 1 full magnitude deeper to reach 500 Myr; see Figure 10), we do not feel that a Monte Carlo simulation of the blue plume presents a promising technique for deriving a recent star formation history either. Nonetheless, we are confident that the present observations carry information relevant to important questions concerning recent star formation in NGC 625. Specifically, is the recent star formation best described as an instantaneous burst, as inferred, for example, in BCDs with strong Wolf-Rayet (W-R) features (Kunth & Sargent 1981)? Recent studies, using updated stellar models, find ages for starbursts in so-called “W-R galaxies” of 3–6 Myr with limits on burst durations of 2–4 Myr (Schaerer, Contini, & Kunth 1999a). Alternatively, is the enhanced star formation better described

as long lived with a lifetime in excess of 10 Myr? Additionally, has the recent star formation been mainly confined to the very center of NGC 625 (or a single star forming region), or has it been distributed throughout the central disk?

In order to answer these relatively simple questions, we will examine the most luminous BHeB stars identified in Figure 11. While there is some “pollution” by reddened MS stars (see below) and a fair degree of uncertainty in magnitude due to the differential reddening, if we examine the BHeB luminosity function in a *statistical* sense and at low temporal resolution (i.e., bin sizes larger than the size of the measured typical reddening vector, 0.5 magnitudes in the V-band), we should be able to construct first-order answers to the above questions. Indeed, we note that, even in nearby low-metallicity systems where differential extinction is expected to be minimal, the observational separation of the MS and BHeB is not perfect, and a statistical separation must be employed (e.g., GR 8, Dohm-Palmer et al. 1998; Sextans A, Dohm-Palmer et al. 2002). Since these investigations have produced reliable star formation histories (note the agreement of the recent SFH derived from BHeB and MS stars in Sextans A, for example), we conclude that the separation of the MS and BHeB sequences in a statistical sense is a robust technique, even considering the strength of differential extinction in this system.

As shown in Figure 10, incompleteness corrections for the BHeB stars should be small for $M_V < -4$, corresponding to unreddened ages $\lesssim 100$ Myr. These relatively massive ($M \gtrsim 5.2 M_\odot$), luminous BHeB stars provide temporal star formation resolution of ~ 25 Myr in this age interval. Since the luminosity of a BHeB star corresponds to a single age (see, e.g., discussions in Dohm-Palmer et al. 1997b, 2002), these blue supergiant stars are excellent probes of the recent star formation history. Thus, by counting the numbers of such stars, and applying conversion factors that account for the IMF and amount of time spent in the BHeB phase, one can glean temporal and spatial information about the recent star formation activity in a galaxy.

We separate the BHeB photometry into four magnitude bins, which correspond to age regions based on the theoretical isochrones of B94: 0-25 Myr, 25-50 Myr, 50-75 Myr, and 75-100 Myr. Figure 11 shows these population regions separated in the BHeB selection box by dotted lines. Note that each selection region has boundaries that follow the slope of the reddening vector ($A_V = 0.6$; see § 5.2). Note also that each region is above the 80% completeness line as derived from artificial star tests, and hence no corrections are necessary.

In Figure 14 we show the spatial distribution of the BHeB stars in these four magnitude bins. The clear separation into identifiable star forming regions in the youngest three epochs indicates that the coarse binning has overcome some of the “noise” introduced by the differential reddening. In particular, the brightest stellar association today (associated with the giant H II region) is seen to be relatively young, while the stellar association to the east appears to be roughly 20-40 Myr older. Furthermore, comparing the highest contour for the 0-25 Myr population (shown in white in Figure 14) with previous star formation peaks, it is clear that star formation has been moving throughout the disk during this time period. Taking these data at face value, it appears that a

prior, stronger burst pervaded the disk 50-100 Myr ago.

Formally, analysis of the coarse BHeB luminosity function implies a large and declining star formation rate over the last 100 Myr. The relative star formation rates (originally in units of $M_{\odot} \text{ yr}^{-1}$, then normalized to unit intensity) over the last 100 Myr are 1.0 ± 0.38 (0-25 Myr), 1.3 ± 0.38 (25-50 Myr), and 5.0 ± 1.3 (50-75 Myr) 5.0 ± 3.8 (75-100 Myr). Errors here reflect Poisson statistics on the number of stars detected in each age bin, as well as average contamination factors as derived from the simulations described below. While we defer more detailed conclusions about the past star formation history of NGC 625 to future investigations where multicolor photometry (e.g., U, B, V, I; see Romaniello et al. 2002) can be used to ascertain detailed spatial information about the dust and to derive line-of-sight corrections for it, this simple model of the recent evolution of NGC 625 should not be dramatically altered. We note that these star formation rates are lower limits, as there will undoubtedly be BHeB stars that suffer little or no differential extinction but undergo photometric errors carrying them blueward of the selection regions here; however, this effect should be independent of magnitude and hence will not drastically alter the *relative* star formation rates for each coarse age bin. We conclude that the average SFR from 100-50 Myr ago was a factor of ~ 5 higher than the average SFR from 50 Myr to the present epoch. This suggests that we may be witnessing the final stages of the extended star formation episode in NGC 625, and that this system may be rightly qualified as a “post-starburst” galaxy.

The contamination of the BHeB population by reddened MS stars is measured self-consistently using the simulations described in § 5.2. Here, the recovered star formation rates quoted above are input into 100 realizations of our synthetic model, which includes differential extinction ($0.0 < A_V < 0.6$ magnitudes). Each model iteration provides an independent output photometry set, and hence an independent measure of the contamination of the four segments of the BHeB selection region by reddened MS stars. The average contamination factors from all 100 iterations (for each age bin) are then added into the total error budget of the star formation rates derived from the BHeB stars as described above. While some level of ambiguity may remain due to the choice of isochrones, we again emphasize that the *relative* star formation rates, with errors, should present as accurate a picture of the recent star formation history of this system as is possible from these data. This simple analysis implies that the burst of star formation in NGC 625 has a relatively long duration (of order 100 Myr) and has been widespread throughout the disk.

Such a scenario is consistent with the other observations of this system which were briefly discussed in § 1. In particular, Bomans & Grant (1998) find diffuse soft (ROSAT 0.1 - 2.4 keV) x-ray emission above the northern side of the disk. The presence of this hot ($\sim 10^6$ K) gas at large distances from the current or recent star formation complexes (~ 1 kpc North and East of complex NGC 625 A) suggests that an active outflow has been at work in this system in recent times. For example, if an average outflow velocity of 100 km sec^{-1} is assumed, only ~ 10 Myr would be needed; even if the average velocity is an order of magnitude smaller, the extended star formation event forwarded above could easily have expelled the gas to this distance. However, in the spectroscopic investigation of the ionized gas by MMHS, no direct evidence of an active outflow

from the current major star formation complex is found. Given that the star formation rate has declined during the last 50 Myr, it appears that this is an ideal system in which to investigate the physical processes that terminate or slow hot gas outflows from major star formation complexes. Further x-ray imaging is under analysis (Bomans et al. 2003), and when combined with deeper multi-color photometry of the starburst regions, we should be able to address this interesting and important issue in greater detail.

The most important conclusion of this star formation history analysis is that NGC 625 appears to have sustained a heightened star formation rate for an extended period of time (i.e., $\gtrsim 10$ Myr). With the aid of this modeling approach, we can easily discern between bursts of star formation that are of short (~ 5 Myr) or long (~ 50 Myr) duration. By comparing our data to various model realizations, we reject any model which does not sustain massive star formation long enough to populate the BHeB region of the CMD. To visualize this, we present in Figure 15 a comparison of two synthetic bursts of star formation; one of short duration (5 Myr), and one of long duration (50 Myr). It is clear that the short-duration burst fails to populate the BHeB region of the CMD, while the longer-duration burst is more successful at placing appreciable numbers of stars in this region. Note also the presence of numerous stars in the color region $(V-I) > 0.1$ in the empirical photometry, and the pronounced dearth of stars in this location in the short-duration burst model. From these tests we conclude that the star formation in NGC 625 is of extended duration compared with most models of starbursts (durations $\sim 3-6$ Myr), and that the presence of spectroscopic W-R features does not rule out a longer-duration star formation event.

7. The Older Stellar Population

Here, we analyze the older stellar populations in NGC 625, namely the intermediate and old age AGB and RGB stars. While the depth of photometry here does not allow the derivation of a quantitative star formation history for intermediate and old ages, we can take a qualitative look at the past evolution of this system.

7.1. The Red Giant Branch

To date, all nearby low-metallicity dwarfs have been shown to contain some fraction of an older stellar population, although in some cases it may be very small (e.g., the very low-metallicity Local Group dwarf Leo A, Tolstoy et al. 1998; Dolphin et al. 2002). This red population appears to be present in all galaxies that are near enough to allow it to be resolved. The spatial distribution of RGB stars is expected to trace the general morphology of a galaxy at the time when the dominant component of its old stellar population formed. By studying the spatial distribution of the older stars, we may hope to attain a basic understanding of the past star formation history of a galaxy. Of course, stellar evolution models become moderately degenerate in age and color on the RGB

after ~ 1 Gyr (i.e., temporal resolution becomes much more difficult than for younger stars in the blue plume), so using such features for quantitative analysis of the past star formation history requires both deep photometry and sophisticated modeling (Dolphin 2002, and references therein). Due to the distance of NGC 625, such an analysis of the RGB is not feasible. Rather, we use these stars to demonstrate the presence of an old stellar population, and use their spatial distribution to understand various facets of the galaxy’s history in a qualitative sense.

A comparison of the RGB stars with the overall H I distribution of NGC 625 demonstrates good agreement. In the analysis of VLA observations of this southern target, CCF00 were unable to unambiguously model the H I mass distribution or to derive a rotation curve. This is due to the highly disturbed and complex H I distribution found in this galaxy, with multi-peaked H I emission and apparent large-scale rotation about the major axis rather than the minor axis. In a large-scale sense, however, the high-column density H I distribution follows the stellar disk of this galaxy quite well, with a nearly east-west major axis that appears to align with the distribution of RGB stars (at least throughout the stellar disk of the galaxy). This agrees with the position angle of the major axis (92°) derived by MMHS. Recall from § 3.2 that we applied elliptical selection regions of axial ratio 2.8:1 to isolate crowding effects in our photometry. These regions closely trace the isophotal contours of the stars, in particular those of the RGB stars in the outer regions of the disk and in the halo. The photometric center of these regions (and of the galaxy) falls very near the center of the stellar disk, nearly equidistant between the H II complexes NGC 625 B and NGC 625 C (α, δ (J2000) = 01:35:05.33, -41:26:09.9). The overall agreement of the H I and RGB distributions suggests that stars have been forming in the present disk-like morphology for a very long time.

7.2. The Asymptotic Giant Branch

The AGB selection region shown in Figure 11 isolates stars that are extremely red in color ($(V-I) > 1.5$ and extending to 3). As this feature is not predominant in all galaxies (see below), its unexpected strength warranted a careful exploration of the errors associated with the photometry of these particular stars. The extremely red colors of some of these stars must, of course, be the result of errors in the $(V-I)$ color index. Indeed, as the limiting magnitude uncertainty is decreased, this extension becomes smaller and less-populated. However, even at the very low error limit of $\sigma < 0.1$ magnitudes in both I and V, the feature is still detected prominently and is therefore robust. Note also that, in Figure 7, most of these AGB stars lie above the 80% completeness lines, suggesting only minor corrections for such effects.

The spatial distribution of these red AGB stars varies relatively smoothly, much like the distribution found for the RGB stars (see § 7.1). However, it is confined closer to the disk of the galaxy than are the red giant stars, again reinforcing the segregation of the various stellar populations based on age. The apparent under-density of AGB stars near the largest star formation region is most likely not real, but is caused by the lower spatial resolution of the WF chip having difficulty with the highly crowded stars in this region, and the relatively under-luminous AGB and

RGB stars being overcome by the more massive and brighter MS and BHeB stars.

The ratio of RGB stars to AGB stars changes as a function of galactic radius. In Table 6 we show this ratio as a function of region (see Figure 6). The ratio falls from values near 40 in the outer regions, which are dominated by RGB stars, to values less than 10 in the central regions, where AGB stars are more prominent. Note that, in the central sections of the galaxy, our sensitivity to these comparatively under-luminous stars drops, as they can easily be overwhelmed by brighter, younger stars. As previously noted, the shape of the RGB and AGB selection regions was chosen to follow the empirical distribution of stars in these regions, as well as the general position and shape of the theoretical isochrones. While the numerical results will be slightly dependent upon the choice of the shapes of these regions, the overall result is quite robust, in that we detect a decreasing number ratio of RGB to AGB stars as a function of decreasing galactocentric distance. We interpret this as verification of the stellar population gradient in NGC 625. The presence of a fairly extended old stellar halo in NGC 625 argues for active star formation in the distant past (c.f., Minniti & Zijlstra 1997). Since AGB and RGB stars both have large and overlapping ranges in age, the AGB to RGB ratio cannot be converted directly into an unambiguous star formation history constraint. However, under the simple assumption that the AGB population is, on average, younger than the RGB population, the gradual increase in the AGB to RGB ratio with decreasing radius suggests a slow decrease in the active area of star formation in this dwarf galaxy. Of course, this ignores possible metallicity dependences in the AGB luminosity function and other ambiguities, but the ratio may be indicating something both simple and fundamental about the history of star formation in NGC 625.

According to the stellar evolution models of B94, at the metallicity of NGC 625, this red AGB region of the CMD is populated only by AGB stars with ages of a few Gyrs that are relatively metal-rich ($Z \gtrsim 0.001 Z_{\odot}$). This suggests that these stars formed from gas which underwent previous metal enrichment by an earlier generation of stars. The strong RGB population is most likely composed of the low-mass siblings of the stars that enriched this gas, implying that star formation was ongoing early in the history of NGC 625, approaching a Hubble time ago. The detection of this morphology agrees with theoretical isochrones for metallicities higher than $0.001 Z_{\odot}$ (B94). Note the general agreement of the extended metal-rich isochrones with the data in Figure 9. These models demonstrate that the bulk of the AGB stars have ages in the range of 2-6 Gyr. The definitive detection of stars which are predominantly old (RGB stars, ages ~ 10 Gyr), middle age (these AGB stars), and young (see § 6) indicates that NGC 625 has been forming stars throughout the entire lifetime of the galaxy (although, for ages $\gtrsim 1$ Gyr, the rate of star formation remains unconstrained).

A similar AGB is seen in several galaxies where deep HST photometry has been extracted. While this feature is weak in most cases, perusing the (V–I) colors of extracted photometry for some local star-forming galaxies, one finds what may be a similar population of stars in Sextans A (Dohm-Palmer et al. 1997b, 2002), VII Zw 403 (Lynds et al. 1998; Schulte-Ladbeck et al. 1999), UGCA 290 (Crone et al. 2002), and NGC 1705 (Tosi et al. 2001). However, undoubtedly the strongest detection

of this CMD feature is found in the Local Group dIrr galaxy NGC 6822. Therein, Gallart et al. (1994) and Gallart, Aparicio, & Vilchez (1996) find a densely populated, red AGB that occupies the color range $0.9 \leq (V-R)_0 \leq 1.7$. The authors interpret this “red tail” as evidence for an intermediate to old stellar population. The red tail found here seems to be quite similar in color and absolute magnitude to that found in NGC 6822. While the above sample surely is not complete (nor is it exclusive), it serves to demonstrate that, in many cases, such a population of intermediate-age stars is a quite common component of a galaxy’s stellar content, and hence, also of its star formation history.

8. The Burst Triggering Mechanism

The mechanisms and physical processes by which star formation begins and is sustained in galaxies are important, but by no means fully understood. In dwarf galaxies in particular, the questions of how star formation begins and proceeds are especially difficult to address, as these objects have no known internal large-scale mechanisms to regularly prompt the process of star formation (e.g., spiral density waves). Evidence is mounting for the importance of environmental factors which may play a crucial role in the evolution of some of these actively star-forming galaxies, requiring an understanding of not only the detailed nature of the ISM but also the nature of the local conditions in which a galaxy is found (see, e.g., SCM03a). We discuss here some possible scenarios for the evolution of NGC 625, an apparently isolated galaxy. Our spatially resolved stellar population information allows us to examine important characteristics such as the correlation between neutral gas and newly formed stars, the size and distribution of star formation regions, and the timescales over which such regions were active in the past.

NGC 625 sits near the edge of the three-dimensional structure of the Sculptor Group (extended along the line of sight; see § 4). It is natural to posit that a nearby Sculptor member may have triggered the rigorous star formation episode that the galaxy is undergoing. The nearest luminous galaxy is ESO 245-005, with a projected (minimum) separation of 190 kpc. ESO 245-005 differs in Galactocentric radial velocity by only 19 km sec⁻¹. This corresponds to a deprojected distance of 580 kpc (using the TRGB distance for NGC 625, and the TRGB distance estimate of 4.43 ± 0.45 Mpc for ESO 245-005 from Karachentsev et al. 2003). Even assuming the minimum separation of 190 kpc, a relative velocity in excess of 1000 km sec⁻¹ would be required for a near passage (≤ 50 kpc, comparable to the distance of the Magellanic Clouds) within the recent past (≤ 100 Myr). This suggests that either dwarf galaxies can trigger starbursts via interactions from distances of order 200 kpc or that ESO 245-005 is not responsible for the present burst of star formation. Note that ESO 245-005 does exhibit a disturbed H I velocity field (CCF00), but one possible explanation is that ESO 245-005 is undergoing a merging of two dwarf systems. Alternatively, it has been suggested that the H II regions concentrated at the ends of the bar are indicative of an interaction (c.f., Miller 1996).

CCF00 posit that NGC 625 may have undergone a merger event recently, but with a non-

luminous (or now-accreted) companion (perhaps an H I cloud). Indeed, there exist many H I clouds coincident with the Sculptor Group, but they display a wide velocity dispersion about the systemic velocity of the group, and none are coincident in both position and velocity with NGC 625 (see Putman et al. 2002). If a merger between NGC 625 and an H I cloud occurred prior to the current star formation event, the elevated gas densities may have been sufficient to trigger the current burst. In addition, the observed abundance ratios (SCM03b; see further discussion below) would be consistent with chemodynamical models of H I infall events (Hensler & Köppen 1999). Similarly, a merger event cannot be ruled out for ESO 245-005, although an interaction between the two galaxies seems unlikely as the catalyst of the current star formation events. Of course, the galaxies may be interacting on longer timescales, and tidal effects cannot be ruled out completely as having had an effect on the current evolutionary status of the two galaxies (see Taylor 1997 for a more complete study of the frequency of companions in such systems).

The highly disturbed H I velocity field (CCF00) and the confused H α kinematics (MMHS) suggest a merger scenario. We do see clues in the combination of our stellar data and the H I which suggest that the main H I and stellar disk of NGC 625 has been warped. Recall the extension of young stars toward the southeast of the stellar disk; this area corresponds to relatively low-column density H I gas, and suggests that the stars therein may have been perturbed gravitationally and carried away from their formation sites. It is then most intriguing that there also exists a low-column density H I extension toward the northwest of the stellar disk (see Figure 1 of CCF00). The symmetry of these potential warps (although note that they are on very different physical scales) might suggest a tidal interaction with an unseen counterpart. While we do not have optical data for this region, such an investigation might prove fruitful for discerning the nature of the apparent interaction which has left its signatures on both the stellar component, as well as the ionized and neutral gas kinematics, of NGC 625.

If the recent burst is not the result of an encounter with a relatively massive companion, what other scenarios could explain the observed characteristics and star formation history? From chemical evolution arguments, we might be able to gain some insight into the nature of the current burst of star formation. SCM03b find a high N/O ratio for the three H II regions studied in NGC 625 (weighted mean $\log(\text{N}/\text{O}) = -1.30 \pm 0.02$; see their Table 2). This is a high value for N/O at this O/H (see compilation in Kobulnicky & Skillman 1996), and could be interpreted as evidence for a long quiescent period preceding the current burst of star formation. During this time, the intermediate mass stars (likely the predominant producers of N) would have time to lose much of their N to the ISM, making it appear comparatively N-rich (Garnett 1990). Skillman, Bomans, & Kobulnicky (1997) find high N/O in Pegasus ($\log(\text{N}/\text{O}) \sim -1.25$), and posit a similar sequence of events leading to the current (albeit very mild) star formation episode. The HST imaging study of Gallagher et al. (1998) confirms that the global star formation rate in Pegasus has been low for the past few 100 Myrs, suggesting that the delayed N mechanism is consistent with observations of this particular galaxy. If this delayed N production scenario is valid for NGC 625 as well, then perhaps the disrupted ionized and neutral gas velocity fields are the result of the current star formation

episode. That is, perhaps we are witnessing the in situ disruption of the disk of NGC 625 by the ongoing starburst activity.

Of course, since we lose temporal resolution of star formation activity after ~ 0.1 Gyr, we cannot discern any scenario which would take such a timescale to leave its observational signature on the galaxy. However, any consistent scenario must account for the recent star formation (i.e., behavior on timescales of Myr), as well as explain the disrupted velocity fields, the large-scale H I distribution, the displaced young stars toward the southeast region of the galaxy, and the overall heightened star formation rate throughout the galaxy.

9. Comparison with Similar Starbursts

9.1. NGC 625 As A Blue Compact Dwarf Galaxy

The class of star-forming galaxies known as BCDs includes low-luminosity systems that have concentrated and rigorous star formation. The first systematic investigation of these galaxies was given in Thuan & Martin (1981), where various criteria (luminosity, spectra and physical size) were used to differentiate between these systems and other low-mass galaxies. Since then, numerous investigations have shown that while these galaxies share certain properties, the class remains somewhat heterogeneous with respect to morphology and other properties (e.g., Loose & Thuan 1986; Papaderos et al. 1996a,b; Doublier et al. 1997; Doublier, Caulet, & Comte 1999; Cairós et al. 2001a,b). Hopkins, Schulte-Ladbeck, & Drozdovsky (2002) find a wide range in current star formation rates in such galaxies spanning nearly five orders of magnitude, with a median value of $\sim 0.3 M_{\odot} \text{ yr}^{-1}$.

More recently, Gil de Paz, Madore, & Pevunova (2003) have produced a statistically large (although not complete) sample of nearby BCDs, with the aim of understanding the properties of this class of galaxy. These authors postulate new selection criteria for classification as a BCD, that are somewhat different and more quantitative than the previous standard of Thuan & Martin (1981). Gil de Paz et al. (2003) suggest that criteria involving the K-band luminosity ($M_K > -21$), peak surface brightness ($\mu_{B,peak} < 22 \text{ mag arcsec}^{-2}$), and color at the peak surface brightness ($\mu_{B,peak} - \mu_{R,peak} \lesssim 1$) be satisfied in order to classify a galaxy as a BCD. While, at present, few dwarf galaxies have measurements of their K-band luminosities, this work provides useful transformations based on the more common (B–R) color index. Using this new definition of BCD, Gil de Paz et al. (2003) note that some traditional BCD galaxies no longer fit these new criteria (notably, II Zw 33 and Tol 1924-416), but for the most part, the galaxies selected with these new benchmarks agree with those selected by Thuan & Martin (1981). The advantage lies in the more quantifiable nature of the selection process.

Given these new selection criteria, does NGC 625 qualify as a bona fide BCD galaxy? Applying the broadband colors found by Marlowe et al. (1997, assuming that the “core” region therein is

representative of the peak surface brightness, and that surface brightness colors scale as do broadband colors), NGC 625 satisfies each of the criteria of Gil de Paz et al. (2003). The system also satisfies the criteria of Thuan & Martin (1981). Finally, as discussed in SCM03b and in § 8, NGC 625 demonstrates spectroscopic properties that are seen predominantly in blue compact dwarf galaxies. Thus, NGC 625 should be added to BCD surveys. With this in mind, it is insightful to compare the properties of NGC 625 with those found in other nearby, well-resolved starburst and BCD galaxies. In Table 7, we present such a comparison, highlighting important characteristics of both the galaxy and its contained starburst region. Note that this list is neither exhaustive nor complete, but rather draws attention to the most commonly-studied systems within ~ 5 Mpc.

Table 7 demonstrates a wide variety of properties among these selected starburst galaxies. Note, for example, the large range in L_X/SFR and $L_{100\mu m}/\text{SFR}$ between otherwise similar galaxies. Systems showing comparable masses, metallicities and current star formation rates show a large disparity in x-ray and FIR luminosities (compare NGC 1569 and NGC 1705). Similarly, systems showing similar x-ray luminosities, masses, and other characteristics differ in global SFR (compare NGC 625 and NGC 1705). Further similarities can be drawn from resolved stellar population studies of these systems; for example, the old stellar populations in NGC 625 and VII Zw 403 are both uniformly distributed (see Figure 12d and Schulte-Ladbeck, Crone, & Hopp 1998), and both show clear evidence of stellar population gradients. Yet, their current star formation rates, FIR and x-ray luminosities differ markedly and somewhat non-intuitively (note that NGC 625 has a higher current SFR and FIR luminosity, but VII Zw 403 outshines NGC 625 in x-rays). This collection of data argues for the importance of detailed studies of these systems to decipher the nature of star formation in active low-mass starburst galaxies.

9.2. NGC 625 As A Wolf-Rayet Galaxy

The spectrum of the dominant H II region in NGC 625 published by SCM03b showed a broad He II $\lambda 4686$ feature with an equivalent width of 5.5 \AA . According to the criteria of Conti (1991), this qualifies NGC 625 as a Wolf-Rayet (W-R) galaxy. As SCM03b presented the first high S/N spectra of the major starburst region, it is not surprising that recent W-R galaxy catalogs (e.g., Schaerer, Contini, & Pindao 1999b) have excluded this system. In the absence of a detailed study of the photometry of its stars, one could infer several properties of the current burst of star formation from its optical emission line spectrum. For example, Schaerer et al. (1999a) find that the bursts of star formation in all W-R galaxies have ages between 3 and 6 Myr with durations in the range 2–4 Myr. Thus, simply the presence of the broad He II $\lambda 4686$ feature in the spectrum implies that the starburst in NGC 625 is recent (age ≤ 6 Myr) and short lived (≤ 4 Myr). While this may be true of the largest H II region in NGC 625, to infer that this is characteristic of the recent global star formation in NGC 625 is at odds with our observations.

Is this true of other well-studied nearby starbursting dwarfs? In several such systems, there appears to be a discrepancy between the ages of the stellar clusters and the ages of the field stars. In

NGC 1569, Hunter et al. (2000) find ages of most of the young star clusters to be less than 30 Myr (the two super-star clusters have ages of ≤ 7 Myr and 10–20 Myr), while Greggio et al. (1998) find that the period of enhanced star formation has lasted for ≥ 100 Myr. In NGC 5253, the ages of the central star clusters range from 1 to 8 Myr, while the central “field” stars are consistent with ages up to 50 Myr (Tremonti et al. 2001). Tremonti et al. suggest that either the field star populations are created without the uppermost IMF (giving the appearance of an older population), or that the clusters older than 10 Myr dissolve into the field. Note that, based on the optical emission line spectrum, Schaerer et al. (1999a) give burst ages for two components of NGC 5253 as 3 Myr and 5 Myr.

In the case of NGC 625, it appears that star formation has taken place at an elevated rate for at least the last 100 Myr and that the sites of the star formation have been both concentrated (like the present dominant H II region) but also spread about the disk (like the older event in the SE). The presence of broad He II $\lambda 4686$ in the dominant H II region (SCM03b) indicates that the star formation that gave rise to *the present exciting association* must have been recent (≤ 3 Myr) and short lived (see arguments in Schaerer & Vacca 1998 and references therein). For example, the H β equivalent width of 235 Å implies an age of 3 Myr, assuming an instantaneous burst model. Thus, if NGC 625 were too distant for a resolved study of its recent star formation, it would be classified as a W-R galaxy, and the star formation in NGC 625 would be characterized entirely by that associated with the dominant H II region. The recent star formation histories of NGC 1569 and NGC 5253 are both consistent with distributed star formation over a period of roughly 100 Myr or more interspersed with the formation of a few clusters. If the bulk of these stars are formed in the field or in associations, then one does not require the solution of dissolving clusters proposed by Tremonti et al. (2001). In sum, the estimates of burst durations and ages implied from W-R star features could potentially be quite misleading in characterizing a burst of star formation in a dwarf galaxy.

Is the distinction between the age and duration of a global burst of star formation in a dwarf galaxy and the age and duration of a single stellar association or cluster in a dwarf galaxy important? We note a number of cases where the difference between a burst duration of 50 Myr and 5 Myr should be considered. For example, Krueger, Fritze-v. Alvensleben, & Loose (1995) modeled only 5 Myr duration bursts when investigating the spectral energy distributions of blue compact galaxies. Longer duration bursts would tend to “dampen” spectral features and lead to lower burst parameter strengths. In cosmological studies of the luminosity functions of galaxies, the degree of “burstiness” affects the slope of the faint end of the luminosity function. Often, short duration bursts are assumed in these types of calculations, and the assumption of a 10 Myr duration is supported by the reasoning that at longer times the type II SNe produced by the burst will heat the ISM preventing any further star formation (e.g., Ferguson & Babul 1998). Since we are now observing bursts in dwarf galaxies where star formation has continued at an elevated rate for several tens of Myr, it would appear that such “self-quenching” is not necessarily an universal property of starbursts in dwarf galaxies. Although many dwarf galaxies may truly have short duration bursts,

the distribution of burst strengths and durations in dwarf galaxies should still be considered an open question.

10. Conclusions

We have presented new HST/WFPC2 imaging of the nearby dwarf starburst galaxy NGC 625. V and I images are used to model the recent evolution of this actively star-forming galaxy. Our single-star photometry, 80% complete to magnitudes of 26.0 (V) and 25.3 (I), extracts information on the relatively luminous stars in this nearby galaxy, and we compare these results to stellar evolution models and simulations to extract quantitative information on the recent star formation history. The well-defined tip of the red giant branch feature in the I-band luminosity function allows us to derive an improved distance to NGC 625 of 3.89 ± 0.22 Mpc, placing it at the distant end of the three-dimensional structure of the Sculptor Group. We use the spatially resolved nature of our photometry to ascertain properties of the star formation in NGC 625 over the past 100 Myr.

There exists a clear and well-defined stellar population gradient in NGC 625. The young, MS stars are tightly confined to the main disk and active star formation regions. The slightly older BHeB stars are somewhat more diffuse than the MS population, and show an interesting extension to the southeast of the main disk. The oldest RGB stars show a relatively uniform, smooth distribution around and within the disk, and are found to the largest galactocentric radii probed in these observations. We note that NGC 625 is embedded in quite a large H I distribution, which continues much further from the disk ($3.4'$, or ~ 6 optical scalelengths; MMHS) than does the stellar population studied here (CCF00). The smoothly distributed red giant population resembles that found in the nearby BCD galaxy VII Zw 403.

There is a strong spatial correlation of H α emission and young, MS stars. The four detected star formation complexes are correlated with MS stars in all cases. We note that our comparative insensitivity to low surface brightness H II regions may bias such a comparison to only the least-reddened stars. We have undertaken radio continuum observations of this system to further probe the nature of potentially embedded star formation complexes.

We have created a new modeling technique to study the effects of differential extinction in resolved stellar populations. We use this model, with fine temporal resolution (10^5 years), to create our selection regions for the BHeB stars. Furthermore, we self-consistently calculate the percentage contamination of the BHeB sequence by heavily reddened MS stars. Finally, we use this modeling to demonstrate the lack of BHeB stars produced by star formation events of short (< 10 Myr) duration. While the generalization of this method will be developed further in a future publication, we note that the current results are in agreement with the extended burst scenario derived using the BHeB stars.

A basic model of the recent star formation in NGC 625, using only the BHeB stars, suggests an elevated but declining star formation rate over the last 100 Myr. While we reserve a detailed

treatment of the recent star formation history for a multicolor dataset, it is clear from these data alone that star formation in NGC 625 was stronger in the recent past ($\sim 50 - 100$ Myr ago) than it is in the current epoch. However, the presence of broad $\lambda 4686 \text{ \AA}$ emission in the spectra of SCM03b suggests vigorous star formation relatively recently (< 6 Myr). Taken together, these points suggest that the use of W-R features to characterize burst ages can be somewhat misleading and should be treated carefully when a color magnitude diagram study of the resolved stellar populations is not available; this point is especially important for galaxies at higher redshift.

The triggering mechanism of the current starburst is not known. We have discussed various scenarios by which the current star formation episode may have begun. While the neutral and ionized gas kinematics certainly suggest a recent merger, no (luminous) companion galaxy is seen near NGC 625. The stellar and H I distributions seem to suggest a warp in the main disk, perhaps a result of the recent accretion of a lower-mass galaxy or H I cloud. If the current burst has not been triggered by a minor tidal interaction, we may be witnessing the in situ disruption of the main disk of NGC 625 by the current star formation episode.

The current major star formation complex, denoted NGC 625 A in Figure 3(a) and Table 4, is not coincident with the H I column density maximum, but rather is slightly displaced toward the end of the stellar and H I disk and lies in an area of lower H I column density. Furthermore, we find young stars spread out over the entire disk, and, in some cases, quite far from the disk. These factors suggest that star formation may have been widespread throughout NGC 625 in the recent past; our simple model of the star formation suggests elevated, widespread star formation over the last 100 Myr at the least.

Interestingly, NGC 625 displays a high value of (N/O), comparable to values seen in BCD galaxies (SCM03b). Those authors interpret this to signify a relatively quiescent (or inefficient) period of star formation prior to the current burst, allowing intermediate-mass stars to enrich the ISM in N compared to the faster-timescale O enrichment expected from high-mass stars. Further investigation of the relation between chemical composition and star formation should shed light on the universality of such quiescent periods leading to N enhancement.

Finally, comparing NGC 625 to other nearby dwarf starbursts shows comparable star formation scenarios over the last 100 Myr. In both NGC 1569 and NGC 5253, star formation appears to have been widespread over the last 100 Myr, with the formation of clusters perhaps signifying concentrated star formation both temporally and spatially. A similar simple model emerges for NGC 625; we find elevated but declining star formation for the last 100 Myr. However, the spectral properties of the major H II region, showing pronounced W-R features, suggest a short duration for the current burst. This discrepancy, in the case of NGC 625, argues for caution in the interpretation of the presence of W-R features as a definitive property of a short-duration starburst episode. Taken together, these lines of evidence argue for the importance of deep, multicolor datasets that allow the derivation of line-of-sight reddening corrections, and therefore accurate spatially resolved star formation histories, of these intriguing dwarf starburst systems.

The authors appreciate the thorough comments of an anonymous referee that helped to improve this work, and thank Abi Saha for beneficial conversations that helped to facilitate the data analysis. Support for this work was provided by NASA through grant number GO-8708 from the Space Telescope Science Institute, which is operated by AURA, Inc., under NASA contract NAS5-26555. We acknowledge support from NASA through LTSARP grant NAG5-9221. J. M. C. is supported by NASA Graduate Student Researchers Program (GSRP) Fellowship NGT 5-50346, and is grateful for the hospitality of the Institute of Astronomy of Cambridge University and the Ruhr-Universität Bochum, where parts of this work were completed. B. W. M. is supported by the Gemini Observatory, which is operated by the Association of Universities for Research in Astronomy, Inc., on behalf of the international Gemini partnership of Argentina, Australia, Brazil, Canada, Chile, the United Kingdom, and the United States of America. E. D. S is grateful for the hospitality of the Institute of Astronomy of Cambridge University during his sabbatical visit. This research has made use of: the NASA/IPAC Extragalactic Database (NED) which is operated by the Jet Propulsion Laboratory, California Institute of Technology, under contract with the National Aeronautics and Space Administration; NASA’s Astrophysics Data System; the SIMBAD database, operated at CDS, Strasbourg, France; and the NASA/IPAC Infrared Science Archive, which is operated by the Jet Propulsion Laboratory, California Institute of Technology, under contract with the National Aeronautics and Space Administration.

REFERENCES

- Allende Prieto, C., Lambert, D. L., & Asplund, M. 2001, *ApJ*, 556, L63
- Aparicio, A., Gallart, C., Chiosi, C., & Bertelli, G. 1996, *ApJ*, 469, L97
- Appleton, P. N., Davies, R. D., & Stephenson, R. J. 1981, *MNRAS*, 195, 327
- Bajaja, E., Huchtmeier, W. K., & Klein, U. 1994, *A&A*, 285, 385
- Bellazzini, M., Ferraro, F. R., & Pancino, E. 2001, *ApJ*, 556, 635
- Bertelli, G., Bressan, A., Chiosi, C., Fagotto, F., & Nasi, E. 1994, *A&AS*, 106, 275 (B94)
- Bomans, D. J., Cannon, J. M., & Skillman, E. D. 2003, *ApJ*, in preparation
- Bomans, D. J. & Grant, M.-B. 1998, *Astronomische Nachrichten*, 319, 26
- Bureau, M. & Carignan, C. 2002, *AJ*, 123, 1316
- Cairós, L. M., Vílchez, J. M., González Pérez, J. N., Iglesias-Páramo, J., & Caon, N. 2001a, *ApJS*, 133, 321
- Cairós, L. M., Caon, N., Vílchez, J. M., González-Pérez, J. N., & Muñoz-Tuñón, C. 2001b, *ApJS*, 136, 393
- Calzetti, D. 2001, *PASP*, 113, 1449
- Calzetti, D., Meurer, G. R., Bohlin, R. C., Garnett, D. R., Kinney, A. L., Leitherer, C., & Storchi-Bergmann, T. 1997, *AJ*, 114, 1834
- Cannon, J. M., Skillman, E. D., Garnett, D. R., & Dufour, R. J. 2002, *ApJ*, 565, 931
- Carozzi, N., Chamaraux, P., & Duflot-Augarde, R. 1974, *A&A*, 30, 21
- Conti, P. S. 1991, *ApJ*, 377, 115
- Côté, S., Carignan, C., & Freeman, K. C. 2000, *AJ*, 120, 3027 (CCF00)
- Crone, M. M., Schulte-Ladbeck, R. E., Greggio, L., & Hopp, U. 2002, *ApJ*, 567, 258
- Da Costa, G. S. & Armandroff, T. E. 1990, *AJ*, 100, 162
- de Vaucouleurs, G., de Vaucouleurs, A., Corwin, H. G., Buta, R. J., Paturel, G., & Fouque, P. 1991, Volume 1-3, XII, 2069 pp. 7 figs.. Springer-Verlag Berlin Heidelberg New York
- Dohm-Palmer, R. C. et al. 1997a, *AJ*, 114, 2514
- Dohm-Palmer, R. C. et al. 1997b, *AJ*, 114, 2527

- Dohm-Palmer, R. C. et al. 1998, AJ, 116, 1227
- Dohm-Palmer, R. C., Skillman, E. D., Mateo, M., Saha, A., Dolphin, A., Tolstoy, E., Gallagher, J. S., & Cole, A. A. 2002, AJ, 123, 813
- Dolphin, A. E. 2000, PASP, 112, 1397
- Dolphin, A. E. 2002, MNRAS, 332, 91
- Dolphin, A. E. et al. 2002, AJ, 123, 3154
- Dolphin, A. E. et al. 2001, ApJ, 550, 554
- Doublier, V., Comte, G., Petrosian, A., Surace, C., & Turatto, M. 1997, A&AS, 124, 405
- Doublier, V., Caulet, A., & Comte, G. 1999, A&AS, 138, 213
- Drozdovsky, I. O., Schulte-Ladbeck, R. E., Hopp, U., Greggio, L., & Crone, M. M. 2002, AJ, 124, 811
- Dutil, Y. & Roy, J. 2001, AJ, 122, 1644
- Falco, E. E. et al. 1999, PASP, 111, 438
- Ferguson, H. C. & Babul, A. 1998, MNRAS, 296, 585
- Ferrarese, L. et al. 2000, ApJ, 529, 745
- Gallagher, J. S., Tolstoy, E., Dohm-Palmer, R. C., Skillman, E. D., Cole, A. A., Hoessel, J. G., Saha, A., & Mateo, M. 1998, AJ, 115, 1869
- Gallart, C., Aparicio, A., Chiosi, C., Bertelli, G., & Vilchez, J. M. 1994, ApJ, 425, L9
- Gallart, C., Aparicio, A., & Vilchez, J. M. 1996, AJ, 112, 1928
- Garnett, D. R. 1990, ApJ, 363, 142
- Gil de Paz, A., Madore, B. F., & Pevunova, O. 2003, ApJS, 147, 29
- Greggio, L., Tosi, M., Clampin, M., de Marchi, G., Leitherer, C., Nota, A., & Sirianni, M. 1998, ApJ, 504, 725
- González Delgado, R. M., Leitherer, C., & Heckman, T. M. 1999, ApJS, 125, 489
- Heckman, T. M. 1998, ASP Conf. Ser. 148: Origins, 127
- Hensler, G., Dickow, R., Junkes, N., & Gallagher, J. S. 1998, ApJ, 502, L17
- Hensler, G. & Köppen, J. 1999, Astronomische Gesellschaft Meeting Abstracts, 15, 16

- Hodge, P. 1989, *ARA&A*, 27, 139
- Holtzman, J. A., Burrows, C. J., Casertano, S., Hester, J. J., Trauger, J. T., Watson, A. M., & Worthey, G. 1995, *PASP*, 107, 1065
- Hopkins, A. M., Schulte-Ladbeck, R. E., & Drozdovsky, I. O. 2002, *AJ*, 124, 862
- Hummer, D. G. & Storey, P. J. 1987, *MNRAS*, 224, 801
- Hunter, D. A., O’Connell, R. W., Gallagher, J. S., & Smecker-Hane, T. A. 2000, *AJ*, 120, 2383
- Israel, F. P. 1988, *A&A*, 194, 24
- Izotov, Y. I. & Thuan, T. X. 1999, *ApJ*, 511, 639
- Izotov, Y. I. & Thuan, T. X. 2002, *ApJ*, 567, 875
- Karachentsev, I. D. & Drozdovsky, I. O. 1998, *A&AS*, 131, 1
- Karachentsev, I. D., Makarov, D. I., & Huchtmeier, W. K. 1999, *A&AS*, 139, 97
- Karachentsev, I. D. et al. 2003, *A&A*, 404, 93
- Kennicutt, R. C. & Skillman, E. D. 2001, *AJ*, 121, 1461
- Kennicutt, R. C., Tamblyn, P., & Congdon, C. E. 1994, *ApJ*, 435, 22
- Kobulnicky, H. A. & Skillman, E. D. 1995, *ApJ*, 454, L121
- Kobulnicky, H. A. & Skillman, E. D. 1996, *ApJ*, 471, 211
- Kobulnicky, H. A. & Skillman, E. D. 1997, *ApJ*, 489, 636
- Kobulnicky, H. A., Skillman, E. D., Roy, J., Walsh, J. R., & Rosa, M. R. 1997, *ApJ*, 477, 679
- Krueger, H., Fritze-v. Alvensleben, U., & Loose, H.-H. 1995, *A&A*, 303, 41
- Kunth, D. & Sargent, W. L. W. 1981, *A&A*, 101, L5
- Lee, M. G., Freedman, W. L., & Madore, B. F. 1993, *ApJ*, 417, 553
- Lehnert, M. D., Heckman, T. M., & Weaver, K. A. 1999, *ApJ*, 523, 575
- Loose, H. H. & Thuan, T. X. 1986, *Star Forming Dwarf Galaxies and Related Objects*, 73
- Lynds, R., Tolstoy, E., O’Neil, E. J., & Hunter, D. A. 1998, *AJ*, 116, 146
- Madore, B. F. & Freedman, W. L. 1995, *AJ*, 109, 1645
- Marlowe, A. T., Meurer, G. R., Heckman, T. M., & Schommer, R. 1997, *ApJS*, 112, 285 (MMHS)

- Marlowe, A. T., Meurer, G. R., & Heckman, T. M. 1999, *ApJ*, 522, 183
- Martin, C. L. & Kennicutt, R. C. 1995, *ApJ*, 447, 171
- Martin, C. L. 1998, *ApJ*, 506, 222
- Martin, C. L., Kobulnicky, H. A., & Heckman, T. M. 2002, *ApJ*, 574, 663
- Mateo, M. L. 1998, *ARA&A*, 36, 435
- Méndez, B., Davis, M., Moustakas, J., Newman, J., Madore, B. F., & Freedman, W. L. 2002, *AJ*, 124, 213
- Meurer, G. R., Staveley-Smith, L., & Killeen, N. E. B. 1998, *MNRAS*, 300, 705
- Miller, B. W. 1996, *AJ*, 112, 991
- Minniti, D. & Zijlstra, A. A. 1997, *AJ*, 114, 147
- Moran, E. C. & Lehnert, M. D. 1997, *ApJ*, 478, 172
- Papaderos, P., Fricke, K. J., Thuan, T. X., & Loose, H.-H. 1994, *A&A*, 291, L13
- Papaderos, P., Loose, H.-H., Thuan, T. X., & Fricke, K. J. 1996a, *A&AS*, 120, 207
- Papaderos, P., Loose, H.-H., Fricke, K. J., & Thuan, T. X. 1996b, *A&A*, 314, 59
- Puche, D. & Carignan, C. 1988, *AJ*, 95, 1025
- Putman, M. E. et al. 2002, *AJ*, 123, 873
- Ratnatunga, K. U. & Bahcall, J. N. 1985, *ApJS*, 59, 63
- Read, A. M. & Stevens, I. R. 2002, *MNRAS*, 335, L36
- Roberts, T. P. & Warwick, R. S. 2000, *MNRAS*, 315, 98
- Romaniello, M., Panagia, N., Scuderi, S., & Kirshner, R. P. 2002, *AJ*, 123, 915
- Saha, A., Sandage, A., Labhardt, L., Schwengeler, H., Tammann, G. A., Panagia, N., & Macchetto, F. D. 1995, *ApJ*, 438, 8
- Saha, A., Sandage, A., Labhardt, L., Tammann, G. A., Macchetto, F. D., & Panagia, N. 1996, *ApJ*, 466, 55
- Sahu, M. S. & Blades, J. C. 1997, *ApJ*, 484, L125
- Sakai, S. & Madore, B. F. 1999, *ApJ*, 526, 599
- Sakai, S., Madore, B. F., & Freedman, W. L. 1996, *ApJ*, 461, 713

- Schaerer, D., Contini, T., & Kunth, D. 1999a, A&A, 341, 399
- Schaerer, D., Contini, T., & Pindao, M. 1999b, A&AS, 136, 35
- Schaerer, D. & Vacca, W. D. 1998, ApJ, 497, 618
- Schechter, P. L., Mateo, M., & Saha, A. 1993, PASP, 105, 1342
- Schlegel, D. J., Finkbeiner, D. P., & Davis, M. 1998, ApJ, 500, 525 (SFD98)
- Schneider, S. E., Thuan, T. X., Mangum, J. G., & Miller, J. 1992, ApJS, 81, 5
- Schulte-Ladbeck, R. E., Crone, M. M., & Hopp, U. 1998, ApJ, 493, L23
- Schulte-Ladbeck, R. E., Hopp, U., Crone, M. M., & Greggio, L. 1999, ApJ, 525, 709
- Searle, L. & Sargent, W. L. W. 1972, ApJ, 173, 25
- Searle, L., Sargent, W. L. W., & Bagnuolo, W. G. 1973, ApJ, 179, 427
- Skillman, E. D., Bomans, D. J., & Kobulnicky, H. A. 1997, ApJ, 474, 205
- Skillman, E. D., Côté, S., & Miller, B. W. 2003a, AJ, 125, 593 (SCM03a)
- Skillman, E. D., Côté, S., & Miller, B. W. 2003b, AJ, 125, 610 (SCM03b)
- Skillman, E. D., Kennicutt, R. C., & Hodge, P. W. 1989, ApJ, 347, 875
- Skillman, E. D., Terlevich, R. J., Kennicutt, R. C., Garnett, D. R., & Terlevich, E. 1994, ApJ, 431, 172
- Stil, J. M. & Israel, F. P. 2002, A&A, 392, 473
- Storchi-Bergmann, T., Kinney, A. L., & Challis, P. 1995, ApJS, 98, 103
- Summers, L. K., Stevens, I. R., Strickland, D. K. and Heckman, T. M. 2003, MNRAS, 342, 690
- Swaters, R. A. 1999, Ph.D. Thesis, Rijksuniversiteit Groningen
- Taylor, C. L. 1997, ApJ, 480, 524
- Thuan, T. X. & Martin, G. E. 1981, ApJ, 247, 823
- Tolstoy, E. et al. 1998, AJ, 116, 1244
- Tosi, M., Sabbi, E., Bellazzini, M., Aloisi, A., Greggio, L., Leitherer, C., & Montegriffo, P. 2001, AJ, 122, 1271
- Tremonti, C. A., Calzetti, D., Leitherer, C., & Heckman, T. M. 2001, ApJ, 555, 322

van Zee, L. 2000, *AJ*, 119, 2757

van Zee, L., Skillman, E. D., & Salzer, J. J. 1998, *AJ*, 116, 1186

Whitmore, B., Heyer, I., & Casertano, S. 1999, *PASP*, 111, 1559

Zaritsky, D. 1999, *AJ*, 118, 2824

Zaritsky, D., Harris, J., Thompson, I. B., Grebel, E. K., & Massey, P. 2002, *AJ*, 123, 855

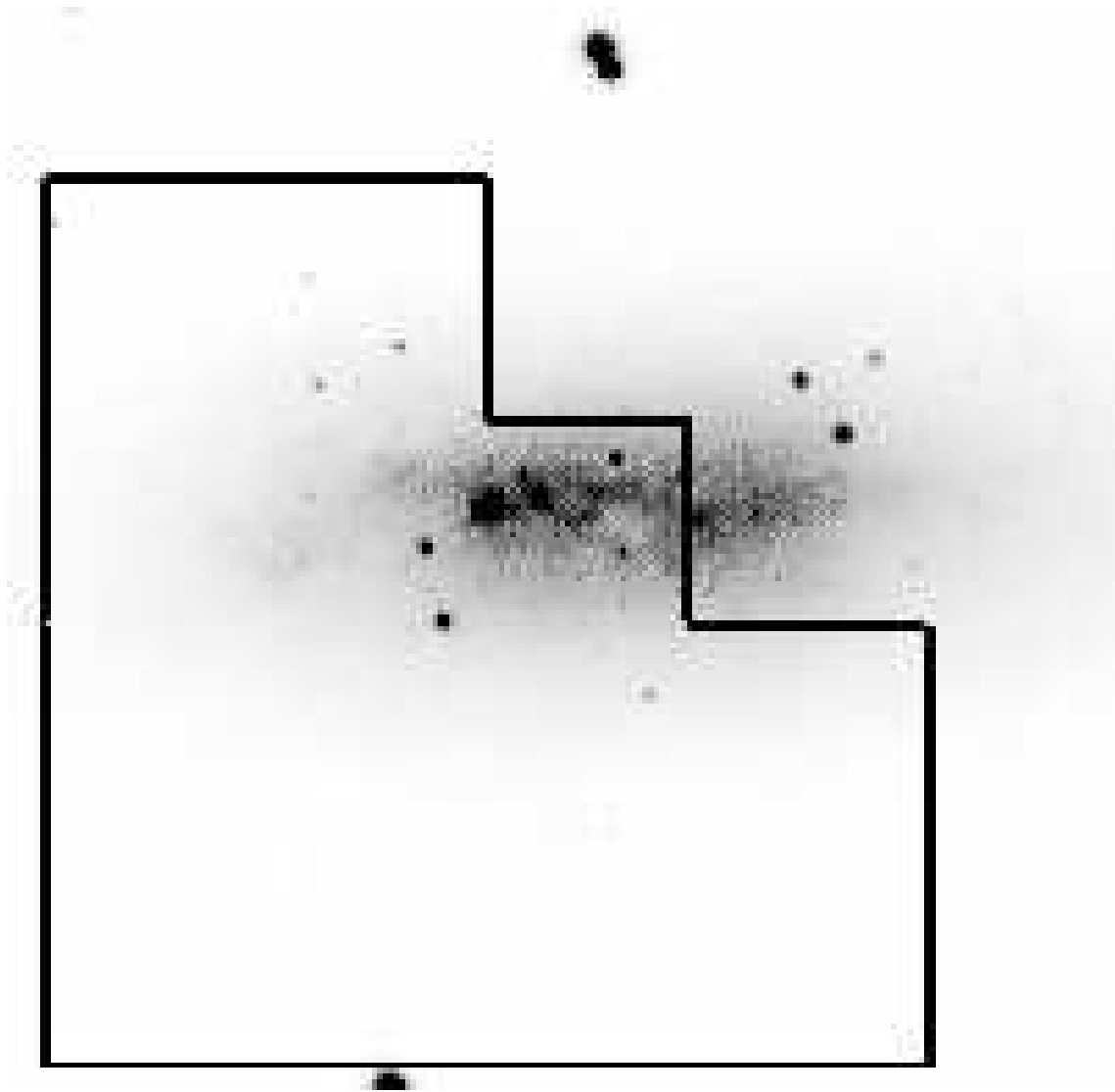


Fig. 1.— Overlay of the HST/WFPC2 field of view on a $4' \times 4'$ R-band image of NGC 625, taken with the EFOSC2 camera at the ESO 3.6 m telescope (October, 2000; P.I. Bomans); North is up and East is to the left. The large star formation region is near the eastern edge of the disk. Central dust concentrations are easily identified, even in this red ground-based image. The implications of this are discussed further in the text. Our chosen orientation and position allows us to sample the starburst region at high resolution (PC chip) while also maximizing our sensitivity to RGB stars away from the disk, aiding in our calculation of the galaxy distance in § 4.



Fig. 2.— 4-color image of NGC 625, created using F555W as blue, $(F555W + F814W)/2$ as green, F814W as red, and F656N as orange. Note the extremely high stellar density throughout the galaxy, and the presence of nebular emission and dust obscuration in the central regions.

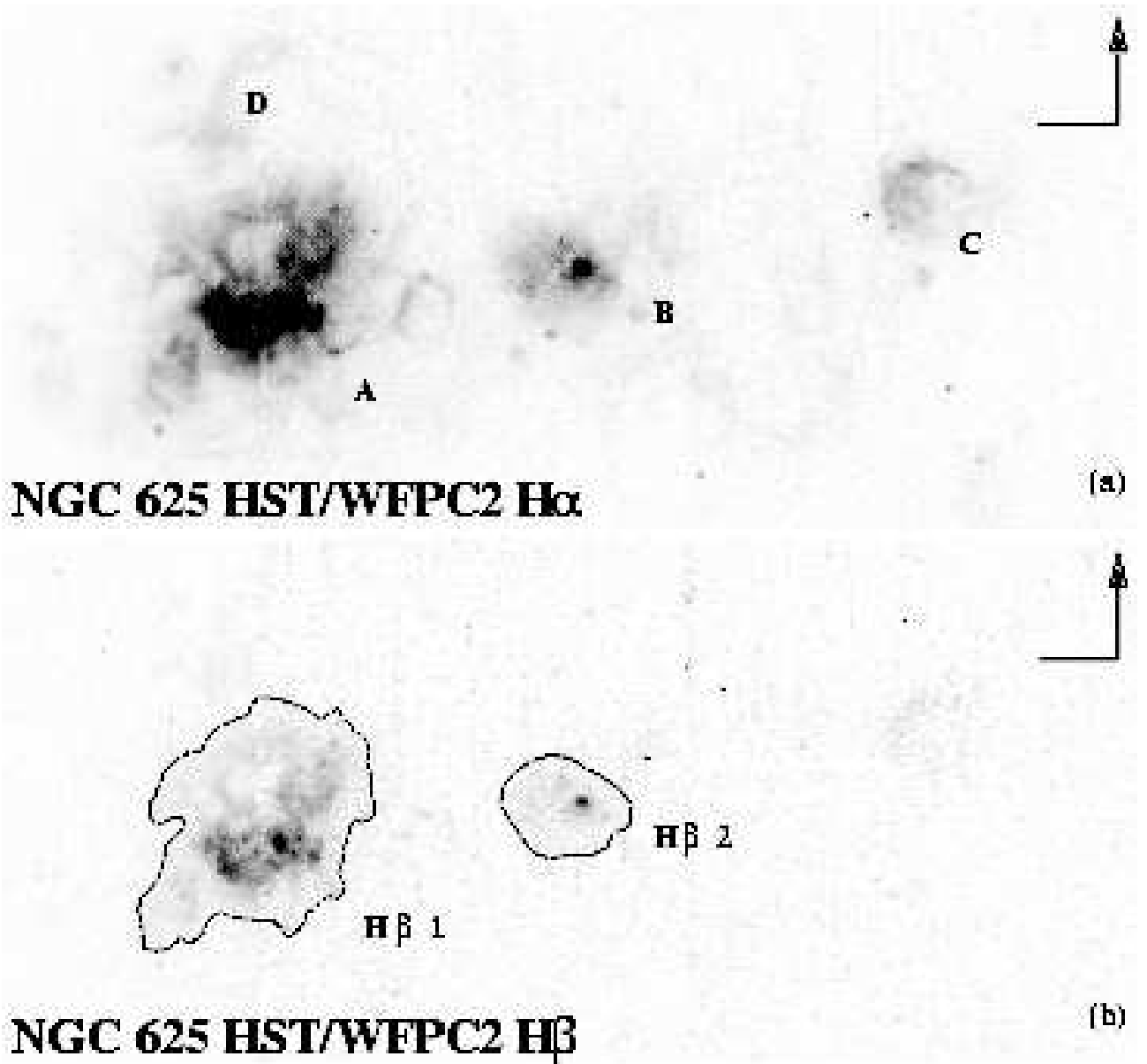


Fig. 3.— Continuum-subtracted images of the central sections of NGC 625, in the lights of H α (a) and H β (b). The field of view, $39'' \times 17''$ ($= 736 \times 321$ pc), is identical in both images; the arrows denote North (tipped) and East. The linear intensity scale ranges from 0 (white) to $\geq 8 \times 10^{-16}$ erg $\text{sec}^{-1} \text{cm}^{-2}$ (black), and is the same in both images. The labels A-D in (a) correspond to the H II regions described in Table 4. The labels H β 1 and H β 2 in (b) correspond to the areas of highest H β equivalent width, listed in Table 5. The lower signal to noise ratio of the H β image limits which sections of the galaxy may be sampled for the effects of internal extinction by using the H α /H β ratio.

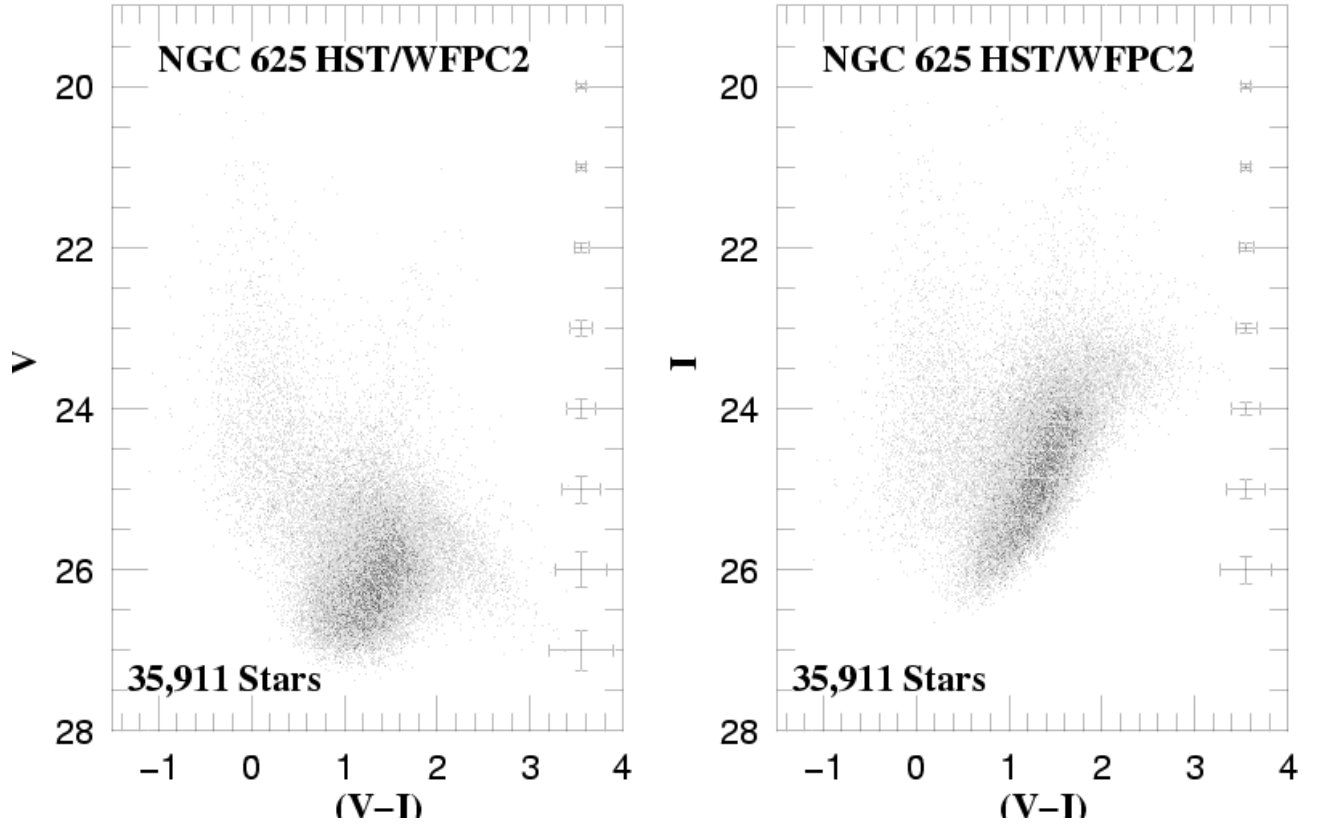


Fig. 4.— Color magnitude diagrams derived from the extracted photometry of NGC 625. (a) shows the V vs. (V-I) CMD, and (b) shows the I vs. (V-I) CMD. All matched stars with total photometric errors < 0.2 mag in both bandpasses are included here (35,911 stars). Average errors in magnitude and color (applying bin sizes of 1.0 magnitude) are included at the right hand side for comparison. Salient features of the CMD are easily identified, including the blue plume and AGB. This very red AGB (or “red tail”) extends to $(V-I) > 2.5$ and is discussed in § 7.2.

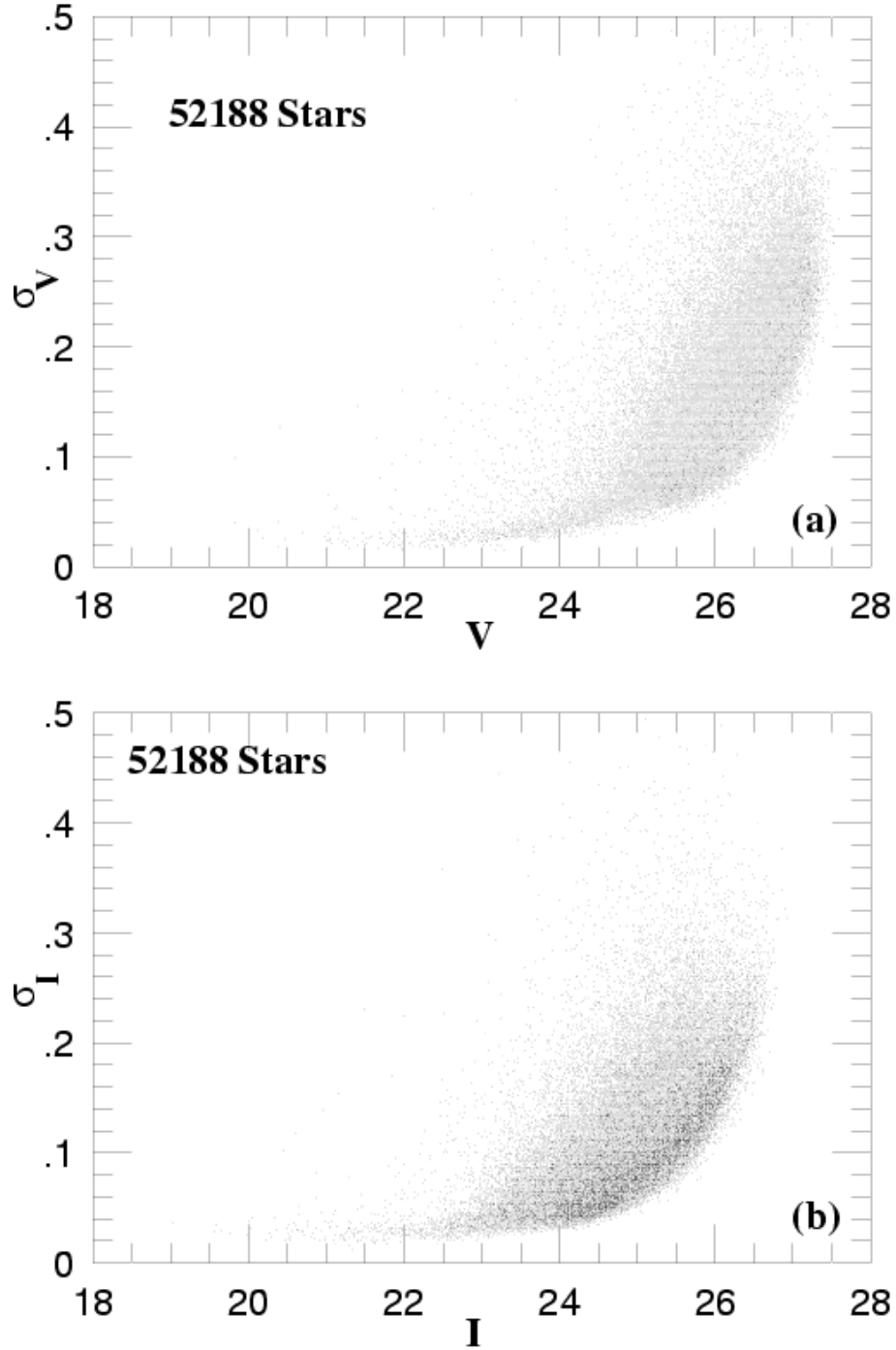


Fig. 5.— DoPHOT internal error distribution for all stars matched between the V-band (F555W filter, a) and the I-band (F814W filter, b). The vertical scatter results from high stellar crowding in some sections of the images. Only stars with photometric errors below 0.2 mag in both I and V are kept in the analysis at hand; this reduces the number of stars to 35911. See § 3 for further discussion.

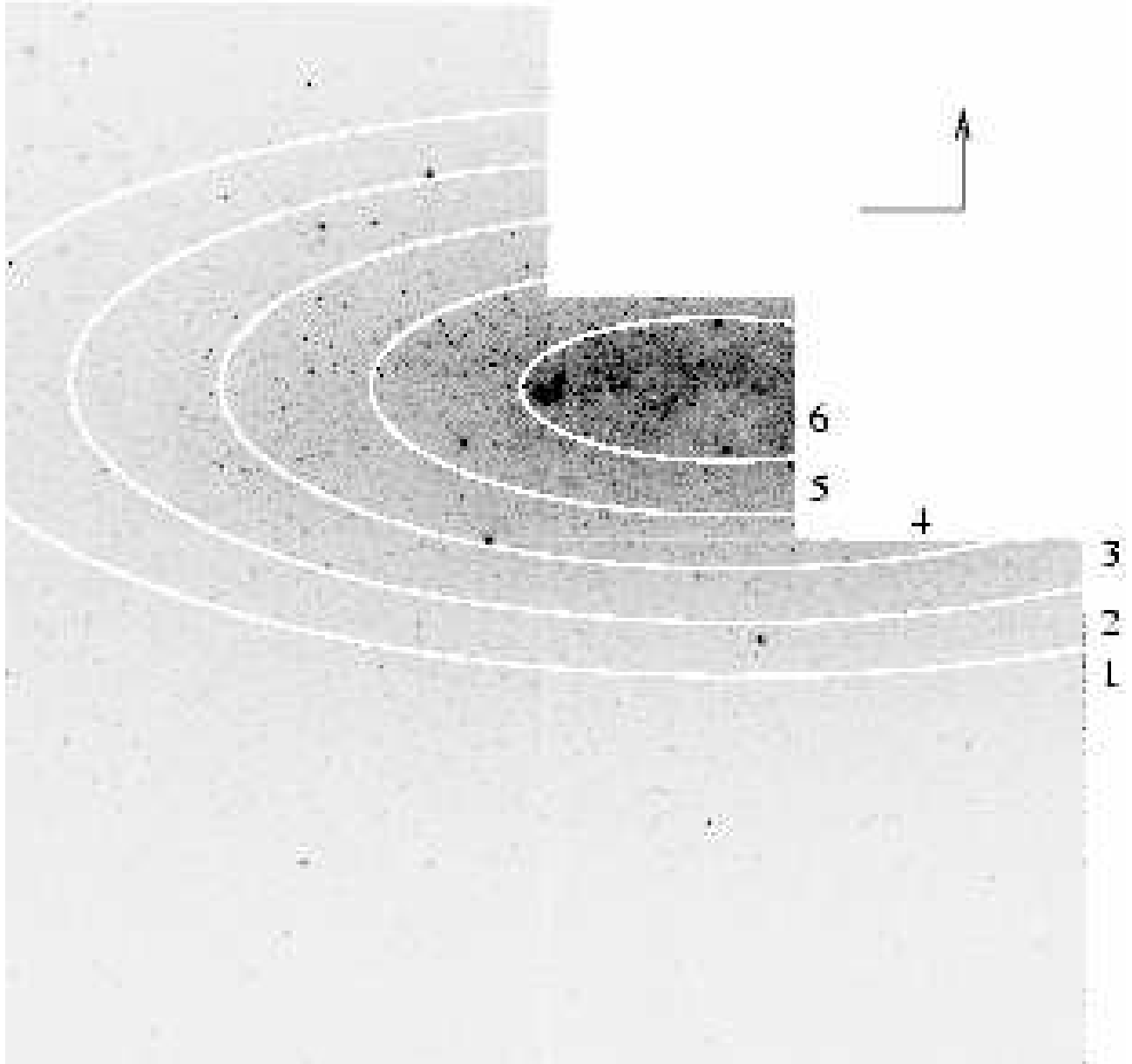


Fig. 6.— NGC 625 in the I Band (10,400 second exposure); the arrows denote North (tipped) and East. The elliptical contours used in the photometric analysis are shown in white; the stellar density increases from Region 1 (essentially halo stars, well separated from the galactic disk) to Region 6 (main disk of the galaxy, including the large H II region NGC 625 A). Individual color magnitude diagrams for each of these regions are shown in Figure 7 and discussed throughout the text.

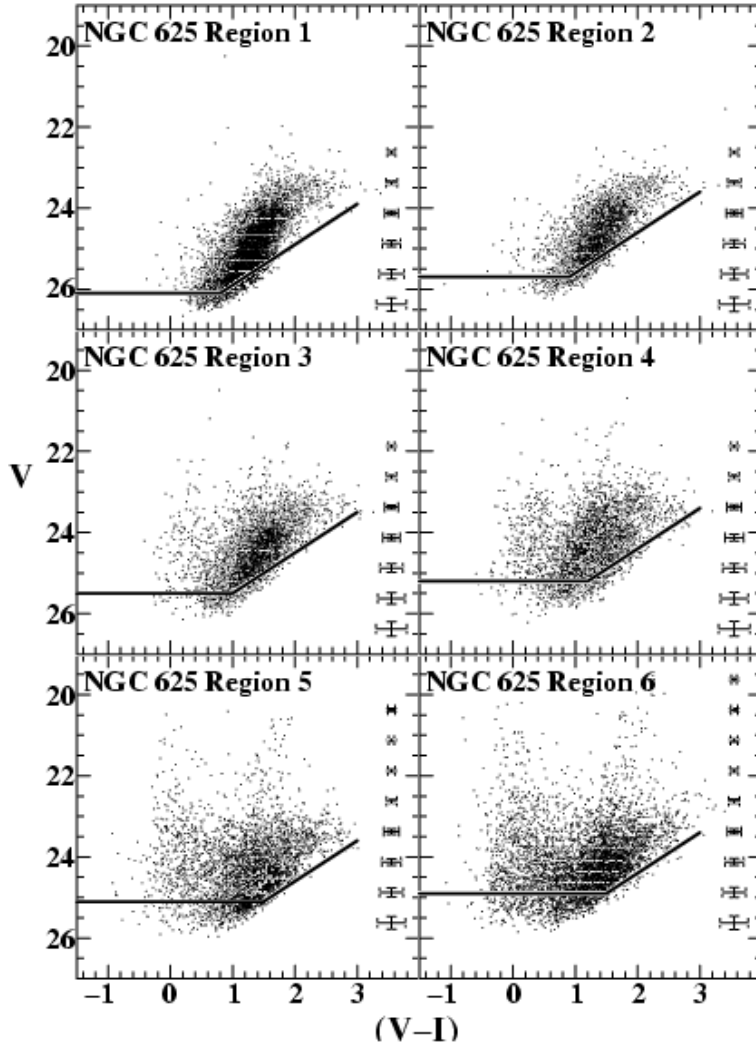


Fig. 7.— CMD’s of each of the separate regions of the galaxy, denoted in Figure 6. The stellar density and crowding are highest in Region 6 (bottom right). Region 1, on the other hand, contains mostly halo stars (red giants) and is used to calculate the TRGB distance (§ 4) and to study the spatial distribution of the old stellar population (§ 7). Note the clarity of the TRGB discontinuity at $M_I = 23.95 \pm 0.07$ (see Figure 8). Only stars with photometric errors < 0.2 magnitudes in both V and I are displayed here and used for the quantitative analysis in deriving the star formation history. The errorbars included at the right in each plot are average photometric and color errors calculated individually for each region, using magnitude bins of 0.75 magnitudes. The thick line in each plot shows the 80% completeness level, as derived from artificial stars tests.

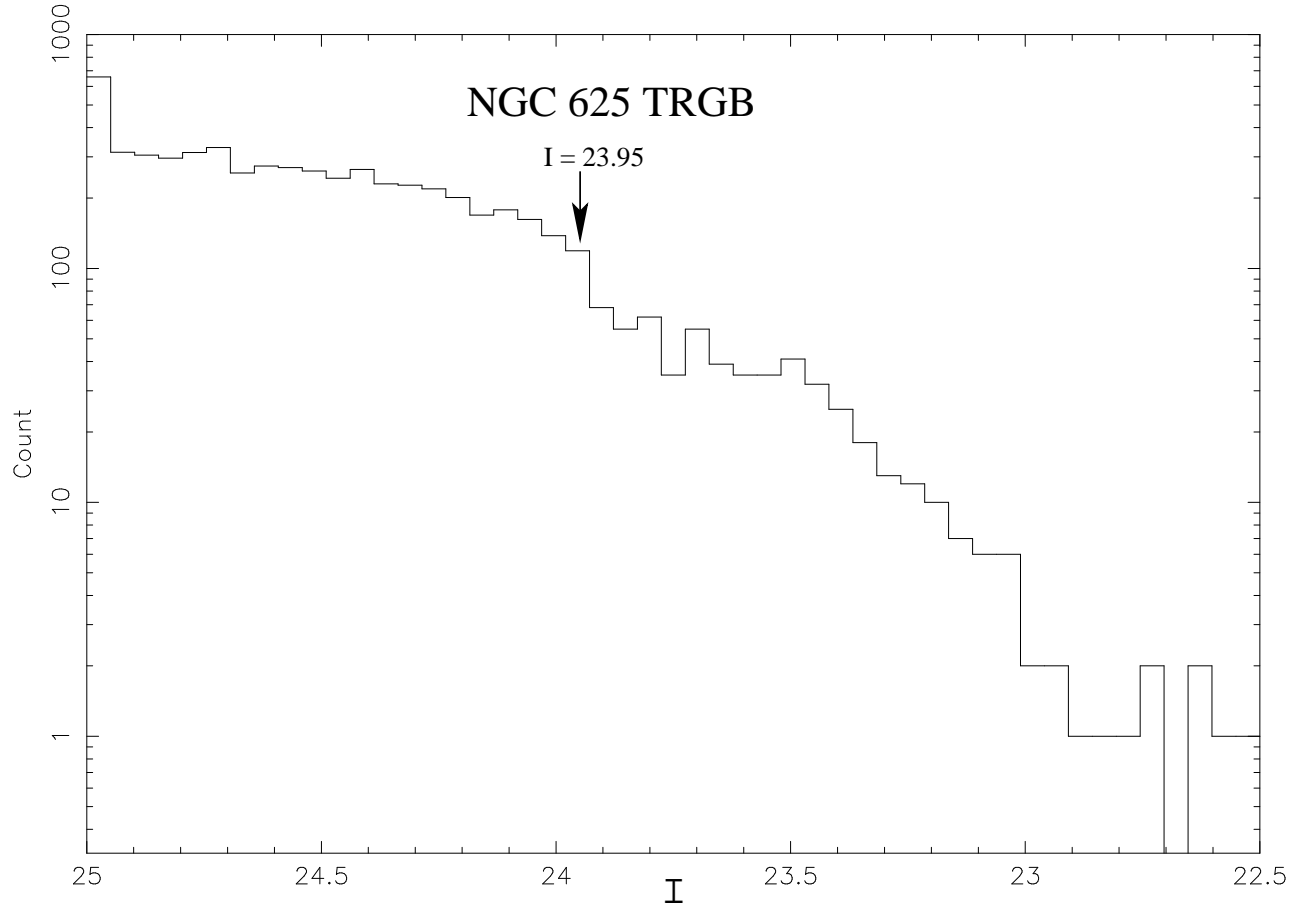


Fig. 8.— I-Band luminosity function of the outer regions of NGC 625 (Region 1 shown in Figures 6 & 7). The position of the tip of the RGB is marked by an arrow at $m_I = 23.95 \pm 0.07$. This value is used to derive the distance to the galaxy, 3.89 ± 0.22 Mpc, in § 4.

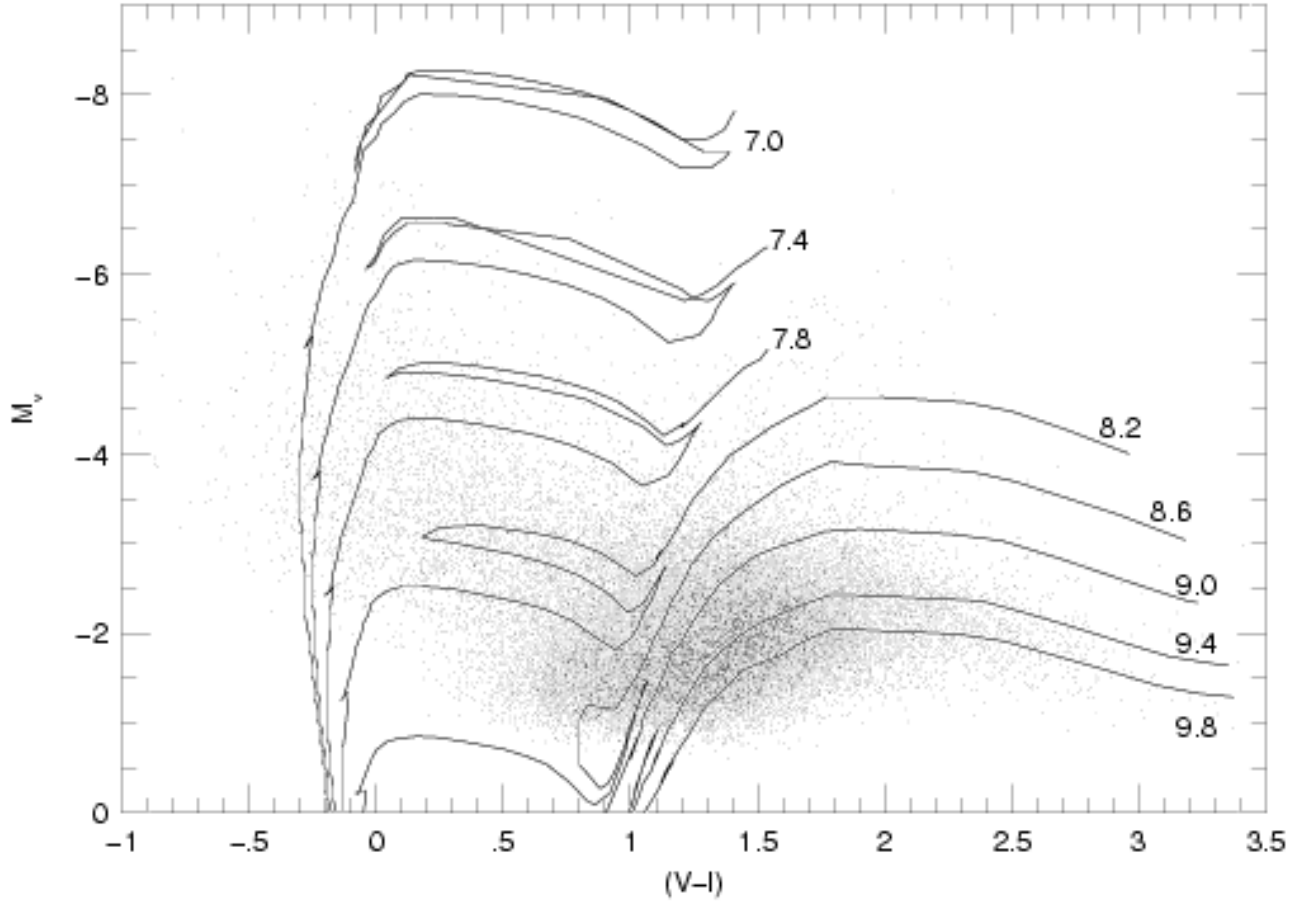


Fig. 9.— $Z = 0.004$ theoretical isochrones from the Padua group (B94) overlaid on the observed V vs. $(V-I)$ CMD of NGC 625. Each isochrone has the logarithm of its age labeled near the largest value in $(V-I)$. Note the extended red AGB stars detected, and the goodness with which the higher-age isochrones fit this feature of the CMD. Lower-metallicity isochrones do not significantly populate this region of the CMD. This suggests the presence of a relatively large intermediate age (\sim few Gyrs) population of AGB stars in NGC 625.

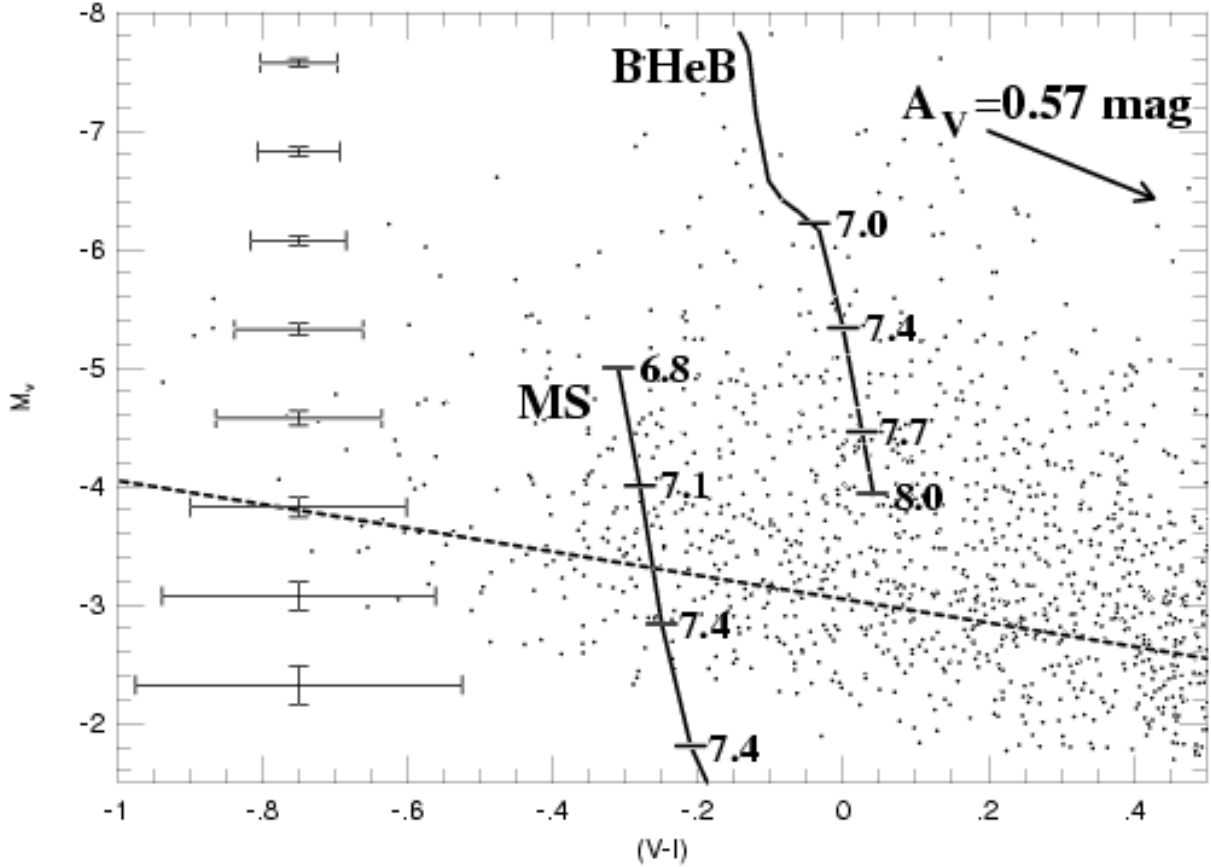


Fig. 10.— Closer view of the blue plume region of the V vs. $(V-I)$ CMD, extracted from the central star formation regions (Region 6; see Figure 6). Overlaid are lines denoting the zero-age MS and the position of the blue extent of the BHeB; tick marks label logarithmic ages. The dotted line shows the 80% completeness level for the Region 6 photometry, as derived from artificial stars tests; note that BHeB stars with ages < 100 Myr are not appreciably affected by incompleteness. The wide color spread of the blue plume, which should only contain these relatively tight sequences of stars, is attributed to large amounts of differential extinction throughout the star-forming regions. The arrow at the upper left indicates the largest reddening detected in our narrow-band imaging (see § 3.3). Since regions of low reddening were also found, the differential extinction is large enough to significantly blur the positions of these stars in the color magnitude diagram, forcing us to apply a statistical separation of these populations.

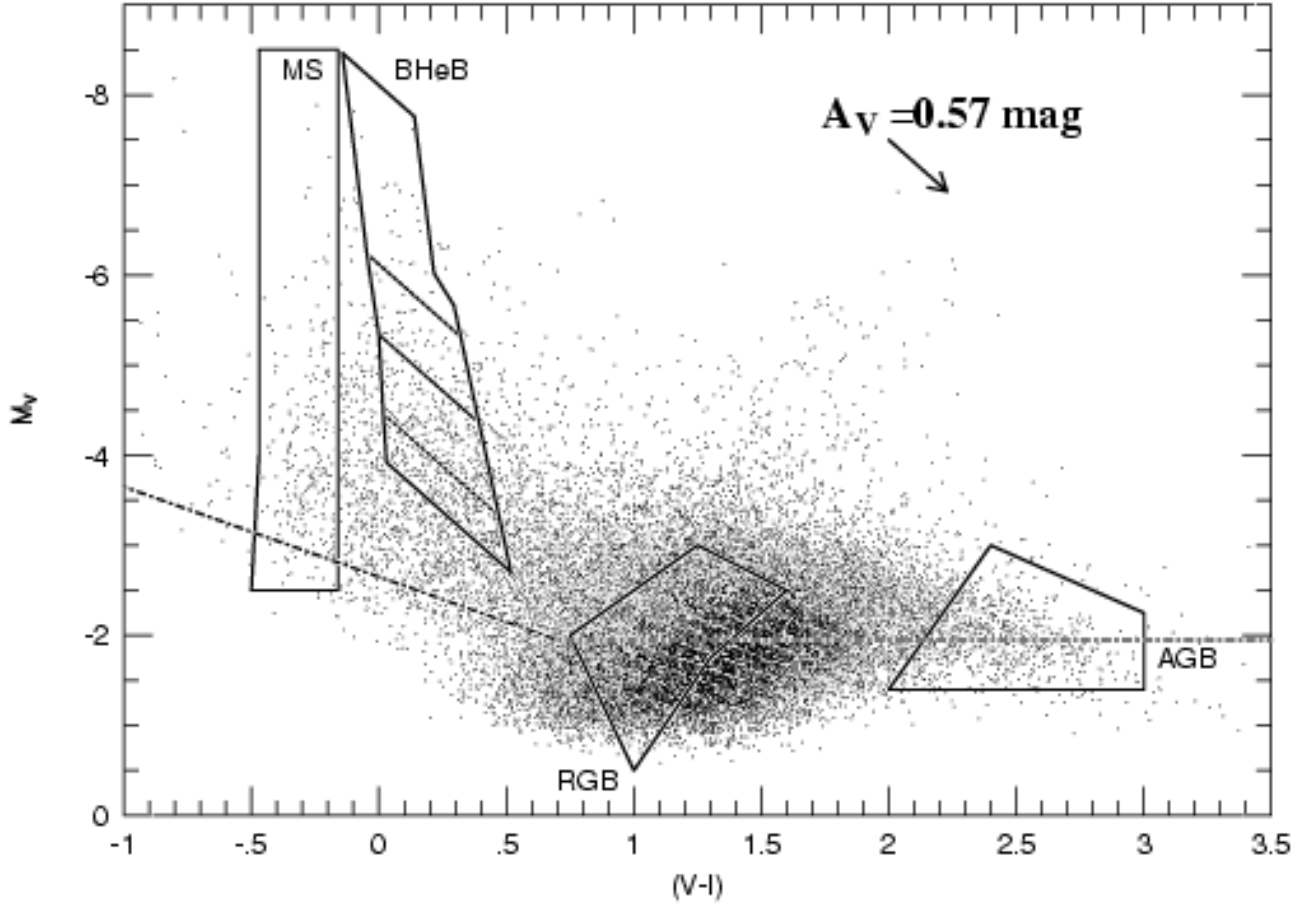


Fig. 11.— The regions of the CMD used to isolate the MS, BHeB, RGB, and AGB populations. The MS and BHeB regions are based on the $Z=0.004$ isochrones of B94; the RGB and AGB regions are created by hand, but follow the empirical distribution of RGB stars and the theoretical and empirical distributions of AGB stars (see discussion in § 5.1). The effects of differential extinction have been modeled as described in § 5.2. The dotted lines in the BHeB sequence represent the borders between the 0-25, 25-50, 50-75, and 75-100 Myr age populations, respectively. Note that these borders follow the direction of the reddening vector. The dot-dash line indicates the 80% completeness level for the entire galaxy, as derived from artificial star tests.

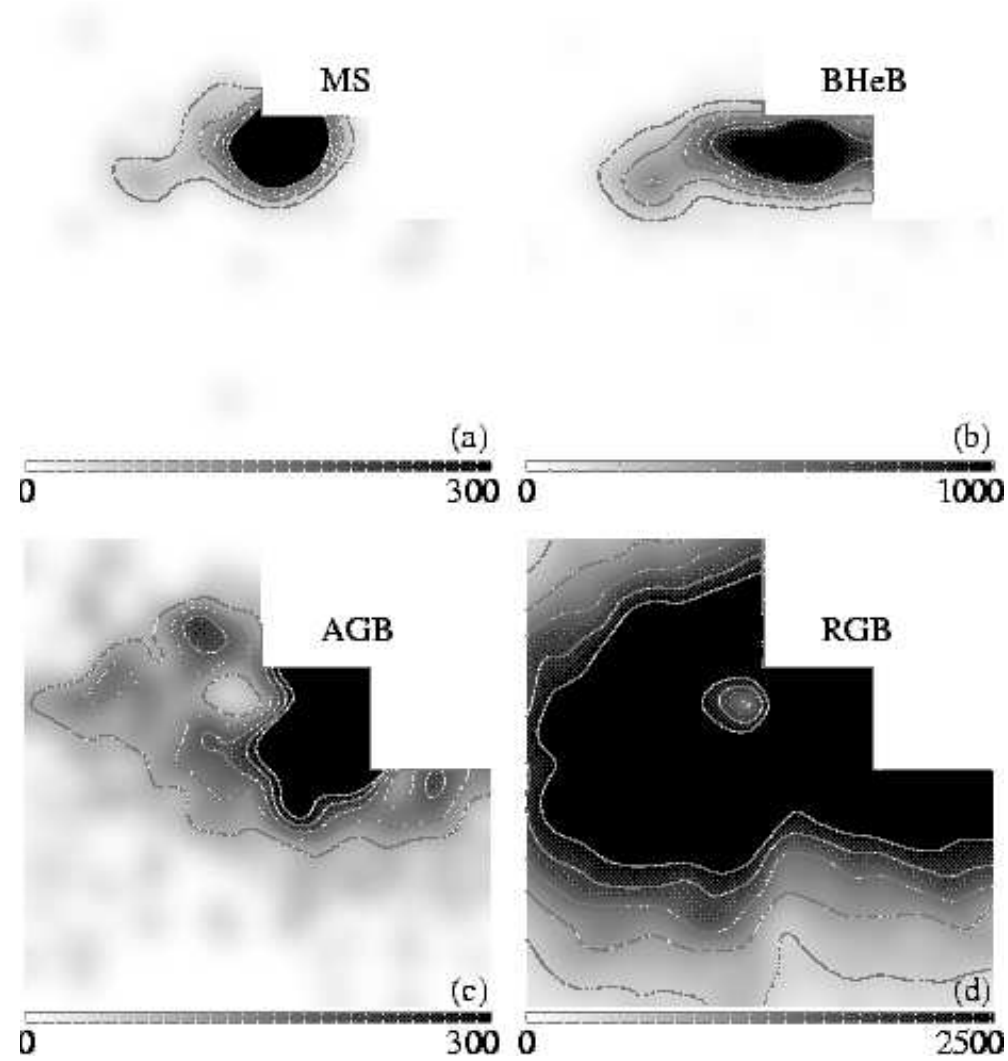


Fig. 12.— Comparison of the spatial distribution of the four different populations of stars studied in NGC 625, extracted using the CMD regions shown in Figure 11. These density plots show the number of stars $\cdot \text{kpc}^{-2}$ for each population, with the color bar below each image denoting intensity. (a) shows the MS stars (contours at 50, 100, 150, 200 & 250 stars $\cdot \text{kpc}^{-2}$), (b) shows the BHeB stars (contours at 150, 300, 450, 600 & 750 stars $\cdot \text{kpc}^{-2}$), (c) shows the AGB stars (contours at 100, 150, 200, 250 & 300 stars $\cdot \text{kpc}^{-2}$), and (d) shows the RGB stars (contours at 500, 1000, 1500, 2000 & 2500 stars $\cdot \text{kpc}^{-2}$). The field of view is identical in all images, with north up and east to the left. Note that the distribution of RGB stars is relatively uniform and diffuse, while the populations grow more compact as one moves toward younger age stars.

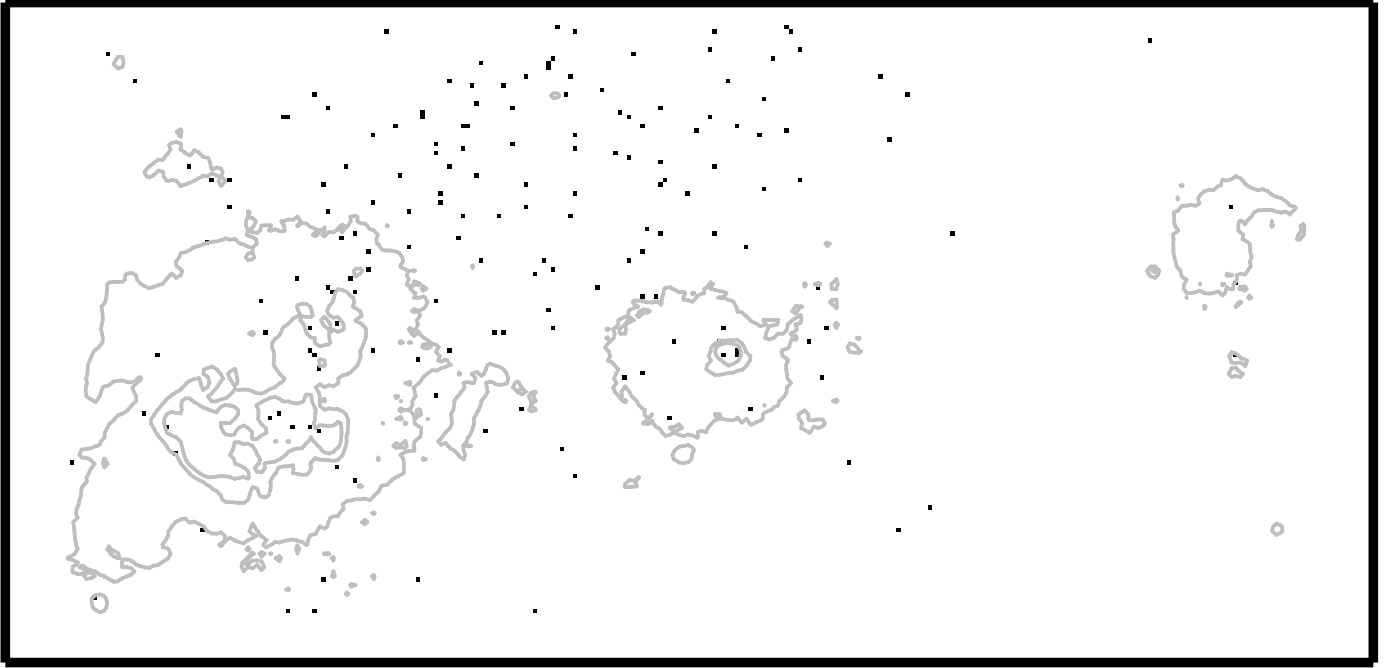


Fig. 13.— Comparison of the spatial distribution of young MS stars ($M_V < -2.5$; black dots) with the morphology of high-surface brightness H α emission (gray contours). The field of view is oriented with North up and East to the left, and is approximately $32'' \times 17''$ (600×320 pc at the distance of 3.89 Mpc derived in § 4). The three large H II complexes are easily identified with those labeled as A, B and C in Figure 3(a). The H α contours are at levels of (1×10^{-16} , 5×10^{-16} , and 1×10^{-15}) $\text{erg sec}^{-1} \text{cm}^{-2}$. Each H II region is identified with present-day MS stars. The improved surface brightness sensitivity of the ground-based imaging of SCM03a demonstrates that diffuse H α emission, not detected here, is found throughout (and slightly beyond) this field of view.

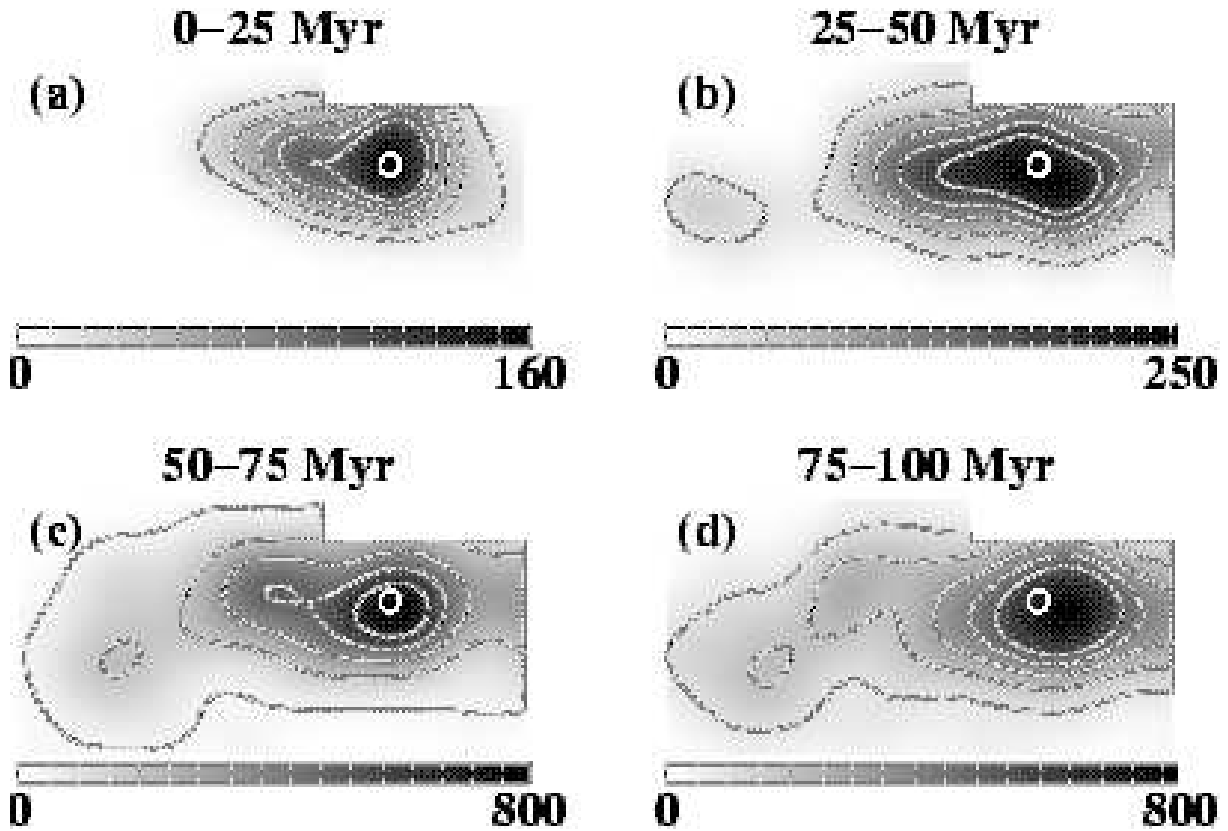


Fig. 14.— Spatial distribution of star formation over the last 100 Myr, as derived from the BHeB stars (see § 6.3). In each plot, the number of BHeB stars $\cdot \text{kpc}^{-2}$ is plotted, with intensities indicated by the color bar under each image; the field of view is $\sim 1.7 \times 0.9 \text{ kpc}$, with North up and East to the left. (a) shows the youngest stars, of age 0-25 Myr; note the concentrated star formation in the main giant H II region; (b) shows stars stars of age 25-50 Myr, and clearly demonstrates that star formation has been occurring in different regions of the galaxy during this epoch; (c) and (d) show older stars, of ages 50-100 Myr, and demonstrate that the star formation rate has been elevated for this entire 100 Myr period. The white circle in each plot is the highest contour for the young, 0-25 Myr population; comparing the location of this peak with past star formation peaks also shows that star formation has been moving throughout the disk over the last 100 Myr. The lowest contour in each plot demonstrates the extent of low-level star formation throughout these epochs. The contour levels (in number of stars $\cdot \text{kpc}^{-2}$) in each image are: (a) 20, 40, 60, 80, 100; (b) 30, 70, 110, 150, 190; (c) 40, 200, 360, 520, 680; (d) 100, 205, 310, 415, 520.

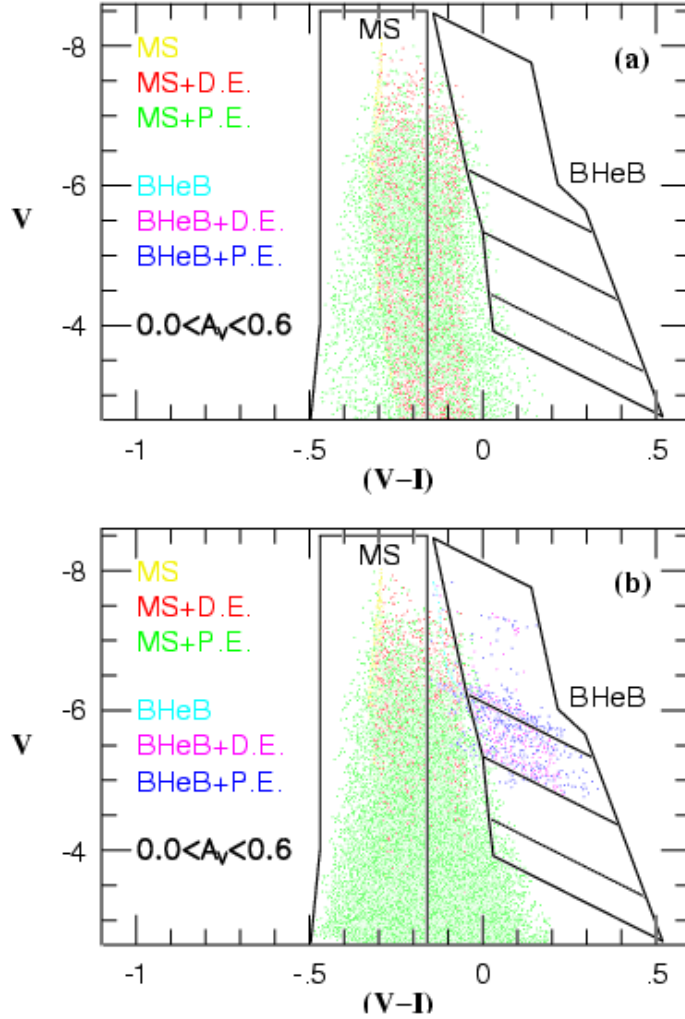


Fig. 15.— Comparison of synthetic bursts of star formation, with equal (constant) star formation rates, but different temporal durations. (a) shows a burst of duration 5.0 Myr (i.e., a standard “short-burst” duration as is typical in models of starburst parameters), while (b) shows a burst of duration 50.0 Myr. Different colors correspond to different evolutionary stages, as labeled; “D.E.” corresponds to differential extinction, and “P.E.” corresponds to photometric errors. The MS and BHeB selection regions are shown in bold lines. The dotted lines within the BHeB regions correspond to the four different age bins (see § 6.3). It is clear that, using the $Z=0.004$ stellar evolution models of B94, no substantial numbers of BHeB stars can be produced unless the star formation event is extended temporally. Comparing to the many empirical stars in the BHeB region of the CMD, we conclude that the star formation in NGC 625 has extended over the last 100 Myr.

Table 1. Basic Properties of NGC 625

Property	Value	Reference	Comments
Mass	$1.1 \times 10^8 M_{\odot}$	CCF00	H I mass only; See § 7.1
V_{Helio}	406 km sec^{-1}	CCF00	
Distance	3.89 Mpc	This work	See § 4
M_B	-16.28	MMHS	
E(B-V)	0.016	SFD98	Foreground only; see § 3.1
$12+\log(O/H)$	8.14	SCM03b	See § 4

References. — CCF00 - Côté et al. (2000); MMHS - Marlowe et al. (1997); SFD98 - Schlegel et al. (1998); SCM03b - Skillman et al. (2003b)

Table 2. HST WFPC2 Observations of NGC 625, Program GO-8708^a

Filter	Emission	Date	Exposure (sec)	Datasets
F656N	H α	2000 Sep 23	800	U64V0207R, U64V0208R
F487N	H β	2000 Sep 23	1200	U64V0205R, U64V0206R
F555W	V-Band	2000 Sep 23	5200	U64V0201R - U64V0204R
F814W	I-Band	2000 Sep 24	10400	U64V0101R - U64V0108R

^aWhen comparing astrometry values derived from these images with other data, we note a 5.1'' offset in declination. The cause of this error is unknown, but the astrometry derived in this paper has been drawn from a coordinate solution using separate imaging. Further use of these data for astrometric purposes should note this difficulty.

Table 3. DoPHOT PSF Shape Parameters and Aperture Corrections

Chip	Filter	FWHM (pixels)	β_4	β_6	β_8	N ^a (Stars)	Residual (rms)
PC	F555W	2.0	7.6	-8.3	3.9	63	0.296
PC	F814W	2.6	7.6	-8.3	3.9	141	0.196
WF2	F555W	1.7	3.6	-1.1	0.4	93	0.162
WF2	F814W	1.9	3.6	-1.1	0.4	274	0.125
WF3	F555W	1.9	3.6	-1.1	0.4	131	0.147
WF3	F814W	2.1	3.6	-1.1	0.4	326	0.122
WF4	F555W	1.8	3.6	-1.1	0.4	107	0.142
WF4	F814W	2.0	3.6	-1.1	0.4	343	0.132

^aNumber of isolated stars which were used to determine the aperture correction. See further discussion in §3.1.

Table 4. The Bright H II Regions of NGC 625

Feature ^a	Center RA (J2000)	Center DEC (J2000)	Diameter ^b (arcsec)	Diameter ^c (pc)	H α Flux (10^{-14} erg sec $^{-1}$ cm $^{-2}$)	L $_{\text{H}\alpha}$ ^c (10^{36} erg sec $^{-1}$)	SFR ^d (M_{\odot} yr $^{-1}$)
NGC 625 A	1:35:06.8	-41:26:13.0	7.2	136	204 \pm 10	3700	...
NGC 625 B	1:35:06.0	-41:26:11.2	3.3	62	112 \pm 6	2000	...
NGC 625 C	1:35:04.9	-41:26:09.3	1.7	32	7.8 \pm 0.4	140	...
NGC 625 D	1:35:07.0	-41:26:05.9	1.2	23	6.6 \pm 0.3	120	...
Total Galaxy	350 \pm 18	6300	5.0×10^{-2}

^aSee Figure 3 for locations. Note that these H II regions (A, B, C, D) correspond, roughly, to regions 5, 9, 18, and 4 in SCM03a. The larger number of H II regions in that study is a result of higher sensitivity to low surface brightness features.

^bEstimated assuming a circular morphology for the H II region; note that, in Figure 3, the apertures used to calculate the flux from each region follow the contours of high equivalent width and are not necessarily circular.

^cCalculated for the TRGB distance derived in § 4 of 3.89 ± 0.22 Mpc.

^dCalculated from the relation $\text{SFR} = (7.94 \times 10^{-42} \text{ erg}^{-1} \text{ sec}) \cdot L_{\text{H}\alpha}$, in units of $M_{\odot} \text{ yr}^{-1}$; see Kennicutt, Tamblyn, & Congdon (1994).

Table 5. Narrow Band Photometry of NGC 625

Feature ^a	H α Flux (10^{-14} erg sec $^{-1}$ cm $^{-2}$)	H β Flux (10^{-14} erg sec $^{-1}$ cm $^{-2}$)	EW(H β) ^b (\AA)	H α /H β Flux Ratio ^c	A $_V$ ^d (mag)
NGC 625 H β 1	180 \pm 9.0	52.6 \pm 2.6	420 \pm 21	3.43 \pm 0.05	0.42 \pm 0.03
NGC 625 H β 2	25.3 \pm 1.3	6.9 \pm 0.3	217 \pm 11	3.64 \pm 0.05	0.57 \pm 0.03

^aSee Figures 3(a) and 3(b) for aperture locations. Note that these regions are smaller than the H II regions characterized in Table 4, and sample only the areas with the highest H β equivalent widths. The low signal-to-noise ratio of the H β image therefore offers the limiting term in our ability to sample internal variations in the extinction properties of NGC 625.

^bAverage value over the aperture, rounded to the nearest Angstrom; errors are assumed at the 5% level.

^cThe error terms account for Poisson errors, the uncertainty in continuum subtraction, and for potential CTE effects across the individual features considered. For a more comprehensive discussion of the individual error terms, see § 3.

^dCorrected for 0.05 mag of foreground extinction (SFD98).

Table 6. RGB:AGB Number Ratios In Photometric Regions

Region ^a	$\sigma(V,I)^b < 0.10$	$\sigma(V,I) < 0.15$	$\sigma(V,I) < 0.20$
Region 1	39.8±6.5	40.1±4.2	51.1±5.0
Region 2	22.2±4.5	25.9±3.3	29.3±3.1
Region 3	31.9±8.1	21.0±2.4	22.5±2.1
Region 4	41.8±18.9	19.3±2.7	16.1±1.6
Region 5	7.4±1.8	8.3±0.9	8.9±0.8
Region 6	8.2±2.2	7.4±0.8	1.5±0.1

^aSee Figure 6 for the location of each region.

^bThe different values of photometric errors in each column correspond to different maximum values of errors in V or I which a given star was allowed to have, and remain in the calculation. So, for example, $\sigma(V,I) < 0.10$ means that all stars have total photometric errors less than 0.1 magnitudes in both V and I. Note that small number statistics begin to affect the error terms for the lowest photometric error cut (e.g., Regions 3, 4).

Table 7. Property Comparison of Selected Nearby Starburst Galaxies

Property ^a	NGC 625	NGC 1569	NGC 1705	UGC 4483	M 82	VII Zw 403	NGC 4214	NGC 4449	NGC 5253
H I Mass (M_{\odot})	1.1×10^8 ^b (1)	1.3×10^8 (2)	1.5×10^8 (3)	3.7×10^7 (4)	7.8×10^8 (5)	3.2×10^7 ^c (6)	1.0×10^9 (7)	$2.3 \times 10^9 \times h^2$ (8)	$\frac{3 \times 10^8}{\sin^2(i)}$ (9)
V_{Helio} (km sec ⁻¹)	406 (1)	-104 (10)	628 (11)	178 (12)	203 (13)	-100 (14)	291 (13)	207 (10)	404 (13)
Distance (Mpc)	3.89 ± 0.22 (15)	2.2 ± 0.6 (16)	5.1 ± 0.6 (17)	3.4 ± 0.2 (18)	3.9 ± 0.4 (19)	4.34 ± 0.07 (20)	2.7 ± 0.3 (21)	2.9 ^d (22)	4.1 ± 0.2 (23)
M_B ^e	-16.3 (24)	-14.9	-16.3 (24)	-12.5	-18.7	-13.7	-16.9	-17.3	-17.1 (24)
Gal. Lat. ($^{\circ}$)	-73.1	11.2	-38.7	34.9	40.7	37.3	78.1	72.4	30.1
E(B-V) ^f	0.016	0.695	0.008	0.034	0.156	0.037	0.022	0.019	0.074
12+log(O/H)	8.14 ± 0.02 (25)	8.19 ± 0.02 (26)	8.0 ^d (27)	7.52 ± 0.03 (28)	$\gtrsim 8.9$ (29)	7.69 ± 0.01 (30)	8.29 ± 0.03 (31)	8.32 ^d (32)	8.15 ± 0.04 (33)
Current SFR ($M_{\odot} \text{ yr}^{-1}$)	0.05 (15)	0.1 ^g (34)	0.1 ^h (24)	0.001 ⁱ (28)	0.7 ⁱ (35)	0.01 ^g (34)	0.1 ^g (34)	0.2 ^g (34)	0.2 ^g (34)
100 μm IRAS Luminosity (10^{36} erg/sec) ^j	140	270	45	Not detected	19000	Not detected	200	Not detected	530
X-Ray Luminosity (10^{36} erg/sec)	100 (36)	800 (37)	120 (38)	N/A	40000 (39)	190 (40)	180 (41)	2500 (42)	650 (43)

References. — 1 - CCF00; 2 - Stil & Israel (2002); 3 - Meurer, Staveley-Smith, & Killeen (1998); 4 - van Zee, Skillman, & Salzer (1998); 5 - Appleton, Davies, & Stephenson (1981); 6 - Carozzi, Chamaraux, & Dufot-Augarde (1974); 7 - Swaters (1999); 8 - Bajaja, Huchtmeier, & Klein (1994); 9 - Kobulnicky & Skillman (1995); 10 - Schneider et al. (1992); 11 - Sahu & Blades (1997); 12 - Karachentsev, Makarov, & Huchtmeier (1999); 13 - de Vaucouleurs et al. (1991); 14 - Falco et al. (1999); 15 - This work; 16 - Israel (1988); 17 - Tosi et al. (2001); 18 - Izotov & Thuan (2002); 19 - Sakai & Madore (1999); 20 - Méndez et al. (2002); 21 - Drozdovsky et al. (2002); 22 - Karachentsev & Drozdovsky (1998); 23 - Saha et al. (1995); 24 - MMHS; 25 - SCM03b; 26 - Kobulnicky & Skillman (1997); 27 - Storch-Bergmann, Kinney, & Challis (1995); 28 - Skillman et al. (1994); 29 - Read & Stevens (2002); 30 - Izotov & Thuan (1999); 31 - Kobulnicky & Skillman (1996); 32 - Skillman, Kennicutt, & Hodge (1989); 33 - Kobulnicky et al. (1997); 34 - Martin (1998); 35 - Lehnert, Heckman, & Weaver (1999); 36 - Bomans & Grant (1998); 37 - Martin et al. (2002); 38 - Hensler et al. (1998); 39 - Moran & Lehnert (1997); 40 - Papaderos et al. (1994); 41 - Roberts & Warwick (2000); 42 - Summers et al. (2003); 43 - Martin & Kennicutt (1995)

^aThe number in parentheses after some entries corresponds to the reference from which that data point was taken.

^bThe H I mass quoted in CCF00 was derived assuming a distance of 2.5 Mpc; the H I mass here has been scaled for the new distance of 3.89 Mpc.

^cDerived assuming the distance listed here, and applying the mass formula, $M_{HI} = 1.7 \times 10^6 \times D^2 M_{\odot}$, where D is the distance to the galaxy in Mpc, given in Carozzi et al. (1974).

^dNo uncertainty quoted

^eDerived from apparent magnitudes listed in NED and using the distances quoted in this table, unless otherwise noted.

^fAll foreground extinction values are taken from SFD98.

^gDerived using the H α fluxes in Martin (1998), and applying the distance in this table and the conversion to SFR from Kennicutt et al. (1994).

^hCalculated using the extinction-corrected total H α luminosity for NGC 1705 found by MMHS and applying the conversion to SFR from Kennicutt et al. (1994)

ⁱCalculated using the total H α fluxes found in Skillman et al. (1994) (UGC 4483) and Lehnert et al. (1999) (M 82), applying the conversion to SFR from Kennicutt et al. (1994), and using the distances given in Row 3 of this table.

^jFluxes drawn from the NASA/IPAC Infrared Science Archive; see <http://irsa.ipac.caltech.edu>. 100 μm luminosity derived using the distance given in this table, and assuming a 30 μm effective bandwidth for the 100 μm filter (i.e., these values will scale with the adopted filter width).